DIPLOMA THESIS

The sensitivity of highly accelerated fMRI to the applied hemodynamic response function model

Virág Darányi

Supervisor: Petra Hermann
assistant research fellow
Brain Imaging Centre
Research Centre for Natural Sciences

BME
2020

MŰEGYETEM 1782

Diplomamunka feladat a Fizikus mesterképzési szak hallgatói számára

A hallgató neve: Darányi Virág	specializációja: Fizikus MSc - orvosi fizika
A záróvizsgát szervező tanszék neve: Nukleáris Technikai Intézet	

A témavezető neve: Hermann Petra - munkahelye: MTA TTK - beosztása: Tudományos Segédmunkatárs - email címe: hermann.petra@ttk.mta.hu	A konzulens neve: Dr. Légrády Dávid - tanszéke: Nukleáris Technikai Intézet - beosztása: egy. docens - email címe: legrady@reak.bme.hu

A kidolgozandó feladat címe: Erősen gyorsított fMRI vizsgálatok érzékenysége az alkalmazott hemodinamikai modellre

A téma rövid leírása, a megoldandó legfontosabb feladatok felsorolása:
Funkcionális MRI mérésekkel nem közvetlenül az agyi aktivitást, hanem az ennek hatására bekövetkező deoxi-hemoglobin koncentráció csökkenést tudjuk mérni, ez okozza a jel növekedését. Ennek az időfüggését általában közelítjük egy általánosan elfogadott "átlagos" válaszfüggvénnyel, de valójában minden emberben, sőt adott emberben minden agyterületen ez eltérő, és az életkorral is változik. Ez hagyományos MRI mérésekben nem okoz nagy problémát, a teljes agy felvétele tipikusan 2-3 másodpercig tart, ez alatt egyszer, esetleg kétszer mintavételezhető ez a válaszfüggvény, azaz az alakjáról túl sok információt nem kapunk. Egy új mérési eljárással azonban a teljes agy felvételi ideje másodperc alá csökkenthető, ami alatt már sokszor mintavételezhető a válaszfüggvény, azaz az adatok kiértékelését várhatóan jobban befolyásoja az alkalmazott hemodinamikai modell.
A hallgató feladata annak vizsgálata, hogy nagyobb időfelbontással mért adatokon az eltérő hemodinamikai modellek alkalmazása milyen hatást gyakorol a kiértékelés eredményére, illetve ennek a hatásnak az összehasonlítása a hagyományos fMRI kísérletekben jelentkező hatással; mind alanyszinten, mind csoportstatisztika esetén.

A záróvizsga kijelölt tételei:

Dátum:

Hallgató aláírása:	Témavezető aláírása*:	Tanszéki konzulens aláírása:	A témakiírását jóváhagyom (tanszékvezető aláírása):

*A témavezető jelen feladatkiírás aláírásával tudomásul veszi, hogy a BME TVSZ 145. és 146.§ alapján az egyetem a képzési célok megvalósulása érdekében a szakdolgozatok, illetve diplomamunkák nyilvánosságát tartja elsődlegesnek. A hozzáférés korlátozása csak kivételes esetben, a dékán előzetes hozzájárulásával lehetséges.

Alulírott **Darányi Virág** a Budapesti Műszaki és Gazdaságtudományi Egyetem fizikus MSc szakos hallgatója kijelentem, hogy ezt a diplomamunkát meg nem engedett segédeszközök nélkül, önállóan, a témavezető irányításával készítettem, és csak a megadott forrásokat használtam fel.
Minden olyan részt, melyet szó szerint, vagy azonos értelemben, de átfogalmazva más forrásból vettem, a forrás megadásával jelöltem.

Budapest, 2020.06.13.

Darányi Virág

aláírás

Acknowledgement

First and foremost, I would like to express my special thanks to Petra Hermann, Ádám Kettinger and Zoltán Nagy, the completion of this thesis could not have been possible without their guidance and assistance.

Furthermore, I wish to thank Zoltán Vidnyánszky and the colleagues of Brain Imaging Centre Research Centre for Natural Sciences for providing the dataset, equipment and expertise that greatly assisted my work.

I would like to express my gratitude towards Máté Kiss and every colleague involved in planning or accomplishing the experiment as well as the participants who took part in the experiment for enabling this work to be possible.

Last but not least, I also thank my family, friends and boyfriend for their unceasing encouragement and support.

Contents

Introduction 1

1. Principles of BOLD fMRI 2
   1.1. The BOLD contrast 2
   1.2. The hemodynamic response 4
   1.3. Resolution of fMRI 5
      1.3.1 Spatial resolution 5
      1.3.2 Temporal resolution 6
   1.4. The sources of noise in fMRI 6
   1.5. Functional MRI data acquisition 7
   1.6. Preprocessing 8
      1.6.1 Motion correction 8
      1.6.2 Spatial normalization 9
      1.6.3 Spatial smoothing 9
      1.6.4 Temporal filtering 10
   1.7. Statistical analysis of fMRI images 10
      1.7.1 General Linear Model 11
      1.7.2 T-statistics 12
      1.7.3 Choice of the HRF model 13
      1.7.4 The Goodness of Fit measures 15
2. Simultaneous Multislice Imaging in fMRI 17
3. Methods 19
   3.1. Data acquisition 19
   3.2. Task paradigm 20
   3.3. Preprocessing 21
   3.4. GLM and the estimated parameters 22
   3.5. Identification of ROIs 24
   3.6. Outcome metrics 25
      3.6.1 Group-level statistics 25
      3.6.2 Subject-level statistics 26
      3.6.3 Goodness of Fit measures 26

4. Results 28
4.1. Goodness of Fit measures 28
4.2. Group-level statistics 31
4.3. Subject-level statistics 34
5. Discussion and conclusion 36
6. Summary 38
References 40
Appendix 44

Introduction

Functional magnetic resonance imaging (fMRI) enables the indirect functional investigation of the brain based on changes in the brain metabolic invoked after neural activation [1]. Nearly all fMRI studies are performed using blood oxygenation level-dependent (BOLD) contrast reflecting the total amount of deoxygenated hemoglobin. In fMRI analysis, the identification of the activated regions in the brain is commonly based on the general linear model (GLM) framework [2]. The change in the BOLD signal intensity evoked by a brief neuronal activity is mathematically described via the hemodynamic response function (HRF). GLM sets up an estimation of the BOLD response using a prespecified HRF model then fits it to the observed fMRI time courses.

Accurate modeling of the HRF is still of great interest in fMRI research, employing various models proposed to achieve this. The emergence of multiband techniques has enabled temporal sampling rates in fMRI acquisition to be significantly higher, even with high-resolution whole-brain coverage [3], [4]. However, the higher temporal sampling can also change the sensitivity to the HRF model misspecification due to the higher number of samples obtained in a single response. The aim of the current thesis is to investigate the interaction between the use of multiband techniques and the choice of the HRF model in GLM fit. For this purpose, I evaluated fMRI datasets obtained with standard EPI sequence with 2-fold in-plane acceleration (GRAPPA) and multiband EPI with two different multiband factors of 4 and 6 using five commonly applied HRF models.

CHAPTER 1

Principles of BOLD fMRI

This chapter is intended to provide a short overview of BOLD fMRI and methods for performing standard BOLD fMRI experiment.

1.1 The BOLD contrast

Unlike methods measuring the direct consequences of neuronal activities, fMRI allows the indirect functional examination of the brain based on the vascular response to the neuronal activation. The activation of a neuron is an energy-consuming process. Due to the intensified energy and oxygen requirements, neuronal activation is followed by increased local blood flow as a consequence of a neurohemodynamic coupling between the two systems. The specific magnetic properties of the blood make the functional imaging of the brain possible via magnetic resonance imaging.

Nearly all fMRI studies are performed using BOLD contrast [5]–[7]. In BOLD fMRI, the functional contrast is based on the effects of the local magnetic susceptibility reflecting the total amount of deoxygenated hemoglobin. Normally, the blood contains a considerable amount of hemoglobin. Hemoglobin has great importance in our metabolism; these molecules perform 98.5% of the oxygen-transport in the blood. Every hemoglobin molecule has magnetic properties that differ according to whether or not it is bound to oxygen [8]. The oxygenated hemoglobin (oxyhemoglobin) is diamagnetic, while the deoxygenated hemoglobin (deoxyhemoglobin) is paramagnetic.

During the fMRI scanning, the diamagnetic oxyhemoglobin does not modify the surrounding magnetic field remarkably. In contrast, the presence of paramagnetic deoxyhemoglobin causes a considerable local field inhomogeneity resulting in more rapid decay of transverse magnetization (T2*) of nearby tissues. The MR pulse sequences sensitive to T2* should show more MR signals where blood is highly oxygenated (i.e., less deoxygenated) and less MR signals where blood is highly deoxygenated [9]. Thus, the intensity of the signal detected in BOLD fMRI (i.e. BOLD signal) reflects the total concentration of the deoxygenated hemoglobin over time.

When a neuron is activated, its energy consumption increases. To satisfy the energy demand, oxygen-rich blood is carried there. The oxygenated hemoglobins sweep out and replace the deoxygenated ones leading to the lower concentration of the deoxyhemoglobin. Owing to this effect, the local field inhomogeneity decreases inducing a small increase (few, 1-5%) in T2* relaxation time and, therefore, in MRI signals. However, the BOLD response has an amplitude comparable to the noise in the data, raising difficulties in the identification of the signal changes evoked by the stimulus. The goal of the BOLD fMRI experiments is to detect such changes in the signal and to make inference about the underlying neuronal activation.

Functional MRI has a major role in neuroimaging. The popularity of fMRI arises from its various advantages (Figure 1) including widespread availability, non-invasive nature, its potential to provide a good balance of spatial and temporal resolution, and its appropriateness for a wide range of experimental questions. These features made fMRI a powerful technique for both research and clinical applications.

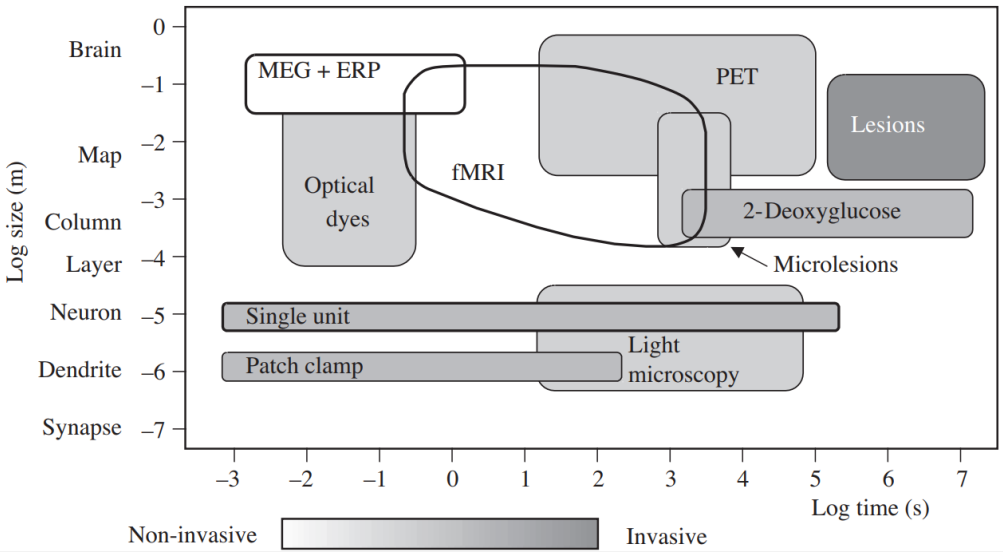

Figure 1. Temporal and spatial resolution of different functional brain mapping methods. Abbreviations: MEG = magneto-encephalography; ERP = evoked response potentials; fMRI = functional magnetic resonance imaging; PET = positron emission tomography (adapted from [2]).

1.2 The hemodynamic response

The change in the BOLD signal evoked by a brief neuronal activity is called the hemodynamic response. As mentioned previously, BOLD fMRI captures the changes in the concentration of deoxygenated hemoglobin from the examined brain region. The amount of deoxyhemoglobin depends on the oxygen extraction of the active neurons and the changes in blood flow and blood volume.

Whereas cortical neuronal responses occur within tens of milliseconds following a sensory stimulus, the hemodynamic response is more extended in time. Due to the changes in the features of the underlying physiological processes (i.e., blood flow, volume, and the deoxyhemoglobin quantity), the hemodynamic response can be divided into distinct phases. Immediately after the onset of the neuronal activity, a decrease known as initial dip appears in the BOLD signal. The initial dip is related to the transient increase in the amount of deoxyhemoglobin attributed to the intensified oxygen consumption of the active neurons. The initial dip is ended by an increase of the signal due to the increased inflow of oxygenated blood. More oxygen is transported to the area than extracted by the active neurons what results in a local decrease in the quantity of the deoxyhemoglobin. The increasing signal intersects the baseline at about 2 s after the onset of the neuronal activity. The maximum of the hemodynamic response (peak) occurs between approx. 4 and 6 s following a brief neuronal activity. If a neuronal activity is not a short-duration event, the peak may be extended into a plateau with slightly lower amplitude than the peak [10]. The return of the signal to the initial baseline is accompanied by an undershoot during the intensity remains below baseline for a prolonged interval. This effect is associated with oxygen metabolism and vascular compliance [8]. An idealized hemodynamic response intensity profile is depicted in Figure 2.

To give an approximate description of the hemodynamic response, some adequate mathematical functions are employed. These functions are usually called hemodynamic response functions (HRF) and correspond to the change in the signal amplitude evoked by a stimulus with instantaneous duration and unit intensity. However, the shape of the response functions is not identical for the whole population, it can vary across subjects, brain regions and stimuli [11] (HRF models are discussed later in Subchapter 1.7.3).

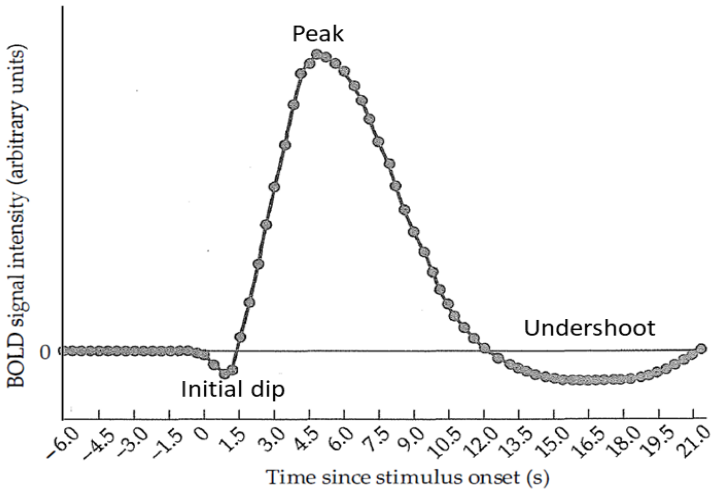

Figure 2. Idealized hemodynamic response (adapted from [7]).

1.3 Resolution of fMRI

Among neuroimaging techniques, functional MRI provides a good balance of spatial and temporal resolution and hence represents an effective technique for a wide range of neuroimaging researches [10]. In this subchapter, I will discuss the factors which determine the spatial and the temporal resolution of an fMRI experiment.

1.3.1 Spatial resolution

The spatial resolution of functional MRI depends on multiple factors. The most obvious parameter is the size of the voxel determined by the following scanning parameters: field of view (FOV), matrix size, and slice thickness. Although splitting the measured volume into smaller spatial elements seemingly should indicate better distinctive functional areas, it results in decreased signal-to-noise ratio (SNR) and expanded acquisition time. On the other hand, a too low spatial resolution could also raise a significant issue called partial volume effect. Singe voxels (even the smallest ones) may contain various tissue types, e.g., white matter, grey matter, cerebrospinal fluid, or blood vessel. Therefore, the measured intensity will contain signal components from tissues not contributing to the BOLD response but to the noise.

Apart from voxel size, there are additional factors that spatial resolution depends on. Since the BOLD signal is controlled by the amount of the deoxygenated hemoglobin, the spatial features of the vascular system (capillaries and veins) also determine the available spatial resolution. Earlier studies found [12], [13] that the vascular system introduces limitations in the spatial resolution of fMRI images. Since blood vessels transporting

oxygenated blood to neurons has a specified spatial extent, a filtering effect will appear on fMRI activation maps. In the best case, the signal is only acquired from the adjacent capillaries of the activated neurons; in the worst case, larger and more distant blood vessels may also contribute to the signal.

In conclusion, the choice of the appropriate spatial resolution for the fMRI experiments is not trivial. One should consider the research questions (e.g., the size of the expected effect evoked by the experimental manipulation) and the previously described spatial characteristics of the BOLD signal. In fMRI measurements, the spatial resolution is typically 3-4 mm, though with higher field magnets (7T) 0.5 mm or less may be obtained [1], [14].

1.3.2 Temporal resolution

Like in the case of spatial resolution, the sampling rate is not the only factor that contributes to the temporal resolution of fMRI. Besides repetition time (TR), the temporal features of the BOLD signal are also crucial. Because of the slow underlying physiological processes, the course of the hemodynamic response takes more than 10 seconds to fade away. As a consequence, the measured fMRI data do not present a snapshot of the neuronal activity but reflects the prolonged changes in the vascular system. Increasing the sampling rate can provide a better approximation of the shape of the hemodynamic response, and thus a better understanding of the underlying neuronal activity [7].

1.4 The sources of noise in fMRI

The most important sources of noise in fMRI measurements are the following [7]:

- thermal noise of the body and the electronics
- system noise of the hardware (e.g., scanner drift)
- head motion
- physiological processes originating mainly from respiration and heart rate
- alternation in the BOLD signal related to non-task related brain processes
- variability in behavioral performance

1.5 Functional MRI data acquisition

There are many valid ways to perform neuroimaging experiments based on fMRI. In the following paragraphs, I will review the steps of conventional fMRI experiments commonly used in neuroimaging studies. I followed these steps during the processing and the evaluation of the data.

During the experiment, a series of volumes is acquired by imaging the subjects' brains while the subjects perform a set of tasks or are exposed to a certain condition. To assure that the results of the experiment will be valid, interpretable, and provide information about the experimental questions, the design of the experiment is a key factor. The experimental design comprises the selection of tasks or conditions and the presentation of stimuli that manipulates the experimental conditions over time. When designing a study, it is crucial to choose an experimental design which suits the research question the most and applying experimental manipulation inducing detectable changes in the signal.

Due to its T2* weighting (i.e., improved sensitivity toward BOLD contrast) and short scanning time, echo-planar imaging (EPI) [15] has become the default fMRI acquisition technique. In a standard fMRI experiment, a single volume with a whole-brain coverage is obtained every few (2-3) seconds. Through the experiments, more than 100 volumes are typically scanned.

The design of the experiment is set up concerning the research questions. In general, the experimental design of fMRI is divided into two major types: block design and event-related design. This grouping is based on the techniques the stimuli are presented. Block design means that stimuli are divided into prolonged task blocks presented to the subject in an alternating pattern. A single block contains only one type of task; the duration of it is about a few 10 seconds. The strengths of this design are its simplicity and high detection power.

In comparison, event-related designs present short-duration stimuli (events) separated with inter-stimulus intervals varying typically from 2 to 20 s. In contrast to the block design, the stimuli may be presented randomly rather than alternately.

Compared to block design, the event-related design enables the application of more complex and flexible experimental designs, which contributes chiefly to the experimental flexibility and growth of fMRI [16]. This design allows for characterizing the shape and the timing of the hemodynamic response providing additional information about the

underlying neural and metabolic processes. However, the event-related design generates smaller changes in the BOLD signal resulting in reduced detection power compared to the block design. Due to the sensitivity to the shape of the hemodynamic response, the analysis of an event-related dataset requires careful choice of the applied model for the hemodynamic response; otherwise, significant activations may be missed [10].

1.6 Preprocessing

The purpose of fMRI studies is to distinguish small, spatially localized variations in the signal evoked by the experimental task. As mentioned in the preceding subchapters, small signal changes corresponding to BOLD contrast are embedded in a noisy signal. Series of procedures applied prior to statistics to remove such an unwanted variability of data and prepare it for statistical analysis are generally called preprocessing. Similar preprocessing algorithm steps are commonly implemented in fMRI experiments due to their less dependence on the experiment design (e.g., block or event-related design). In the following paragraphs, standard preprocessing steps will be reported, which are included in most fMRI analysis packages.

1.6.1 Motion correction

During fMRI experiments, it is critically important to consider the head motion that can introduce severe artifacts into the fMRI analysis. Despite the mechanical restriction (head restraint system), a few millimeters displacements could occur even in the case of collaborating subjects. In voxel-based fMRI analysis, we assumed that each voxel of the time-series is acquired from a unique and unchanging location of the brain. When head movements occur during the measurement, violating the assumption, intensity changes will appear in the images as an additional noise disturbing the detection of the desired response. Motion correction is a standardly applied preprocessing step in fMRI studies. Its purpose is to spatially align the successive volumes in the time series as the brain would have been in the same position during the whole measurement.

1.6.2 Spatial normalization

Regarding human brains, there is remarkable variability in shape and size. Furthermore, the amount of difference may be notably prominent in particular brain regions. This phenomenon raises difficulties in the common evaluation of data obtained from different subjects. Preprocessing step called spatial normalization has been designed to solve this problem. Normalization aims to counteract the variations among individuals by transforming the multi-subject dataset into a standard reference space, enabling the group-level analysis of the dataset. During the transformation, mathematical stretching, squeezing, and warping of the images are carried out. A further advantage is that a common reference space allows the comparison of the data and the results obtained in two or more different studies. A commonly used reference space, called MNI space (Montreal Neurological Institute coordinate space) [17], was constructed by the researchers of Montreal Neurological Institute based on a dataset involving more than a hundred individual anatomical images.

Since a typical functional image appears undifferentiated and blurry, the use of the more detailed anatomical scan as a guide image is beneficial during normalization. To achieve this, prior to the normalization, the functional images are mapped on to an anatomical image obtained from the same subject. This common process is called coregistration.

1.6.3 Spatial smoothing

In fMRI experiments, the application of a low-pass spatial filter is a widespread technique in preprocessing. This process is alternatively called smoothing or spatial smoothing. The main reason for using spatial smoothing is to remove high-frequency spatial components attributed to the noise and as a result of this to enhance SNR. Besides that, spatial smoothing can have additional advantages of improving the validity of statistical methods by decreasing the number of false positive activations and increasing the normality of the error term. The most frequently used spatial filter is the Gaussian filter. In fMRI studies owing to the spatial characteristics of the BOLD signal, the typical value of full width at half maximum (FWHM) of the kernel is about 5 to 10 mm.

1.6.4 Temporal filtering

In fMRI measurements, additional components of very low frequencies are observed in the time series of the measured data. These changes are associated with scanner drift arising from the temporal scanner instability. These effects often appear as nearly linear increasing or decreasing trends in the signal. This low-frequency noise can disturb the detection of the brain response of the experiments. High-pass filtering is a generally used approach in attenuating slow drift-like trends.

1.7 Statistical analysis of fMRI images

After the preprocessing of the dataset, further analyses are performed to determine the brain regions activated by the stimulation. To identify the weak BOLD response in the noisy signal, a careful statistical analysis is required. A commonly used approach is the hypothesis or significance test. The experimenters set up a research hypothesis that makes predictions about the experimental data and a null hypothesis rejecting the former. In fMRI, a general research hypothesis is that the experimental manipulation (e.g., a task or a particular condition) affects the fMRI signal. The goal of the hypothesis test is to evaluate whether the data reflects the effect of the manipulation or the null hypothesis can be accepted.

The output from such a hypothesis-driven analysis is a probability level that the observed data could occur under the null hypothesis. Voxels whose probability levels are below a threshold probability are declared significant, indicating activation in response to the manipulation [10]. Two different types of errors can occur in a hypothesis test. Errors are referred to as false positive (or Type I error) when a non-significant effect is labeled as significant and false negative (or Type II error) when a significant effect is not identified as significant.

In fMRI experiments, the analysis of the data from multiple subjects typically involves two phases performing tests at two levels. These phases are called first- and second- or group-level. In the first-level analysis, the effects are tested at the single subject-level. The output of the first-level then serves as an input into the group-level analysis. The term group-level indicates an across-subjects analysis. Statistical analyses are commonly performed voxel-by-voxel in the whole brain referred to as a whole-brain analysis, or in a selected area known as the region of interest (ROI) analysis.

In fMRI experiments, it is most general to process each voxels' time course individually [2]. This approach is called univariate analysis. It assumes there is no covariance across voxels; any observed covariance is considered as noise. However, there exist also multivariate methods allowing the joint analysis of all voxels by taking into account the spatial relationships across them. In this study, the analysis of the dataset was carried out in a univariate way.

1.7.1 General Linear Model

General linear model (GLM) analysis denotes a collection of statistical methods. It assumes that the observed data series is composed of a linear combination of different model factors along with additive Gaussian noise. In fMRI studies, GLM has become the prevalent statistical framework; nearly every hypothesis testing is based on GLM. All major fMRI statistical packages include routines for performing general linear modeling.

In fMRI analysis, general linear modeling generates a model of the predicted BOLD response and fits that to the observed time series for the whole session. The model consists of a linear combination of independent predictions (i.e., regressors or model factors) that together predict the expected BOLD response. The basic formula for linear modeling for a single voxel is:

$$y(t) = \sum_{i=1}^{n} \beta_i x_i(t) + c + e(t) \quad (1)$$

where y(t) is the observed time series; $x_i(t)$ represents the i-th regressor, n is the number of the applied regressors. The terms β_i (i = 1…n) are unknown parameter weights reflecting the relative contribution of the corresponding regressors ($x_i(t)$) to the observed time series. The letter c expresses a constant term corresponding to the intensity of the baseline in the data, and e(t) is the error term unexplained by the model.

The relationship between a stimulus and its BOLD response is commonly modelled by convolving the stimulus function with the HRF. The use of two or more types of stimulus as well as a complex HRF model comprising multiple basis functions may appear in the equation as additional regressors. (Subchapter 1.7.3 describes the HRF models and their basis functions in more detail.)

Equation 1 is typically expressed in matrix formulation by

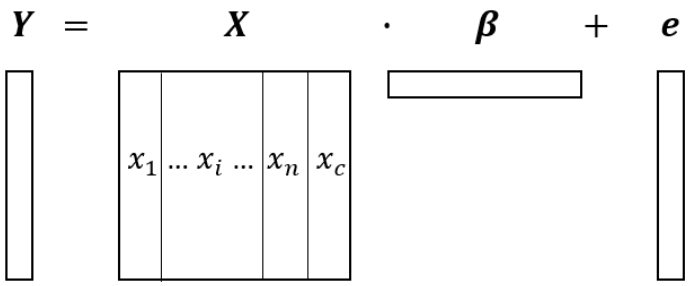

(2)

where **Y** is a vector containing the measured data, **X** is generally referred to as the design matrix containing time courses of regressors by columns, **β** is a vector containing the parameter weights (i.e. parameter vector), and **e** is called error vector containing the unexplained component of the fMRI signal. The constant term (introduced in Equation 2) is involved in the design matrix by an additional column vector of ones (x_0), the parameter weight (β_0) corresponds the baseline level of the measured data.

This equation system (Equation 2) is typically overdetermined, because the number of observations (i.e. number of successive volumes in the time series) is substantially higher than the number of regressors. A widespread solution of such an overdetermined system (i.e. of linear equations) is to assess the combination of β_i values that minimize the sum of the squared residuals. GLM is usually applied in a univariate way; the parameter weights, the constant term, and the residual term are determined independently for all voxels.

1.7.2 T-statistics

The calculated parameter weights only approximate the intensity of the relative signal induced by a given experimental manipulation. To determine whether a particular voxel exhibits activation for a specific manipulation or there is a significant difference between the effects of different manipulations, a suitable statistical method is needed. A common approach is to compare the effect size to its standard error [2]. This method is called t-statistics resulting in a so-called t-score (or t-value):

$$T = \frac{\text{effect size}}{\text{standard error}} \tag{3}$$

The higher the magnitude of t-score, the more significant the effect is. To each t-score a p-value can be assigned which expresses the probability that the results are occurred by chance. P-values are generally determined by comparing the results with a t-distribution with the proper degree of freedom (i.e. number of independent observations). Voxels whose probability does not exceed a threshold probability are considered to be statistically significant (i.e. activated).

T-statistic can be applied in the first and the second-level voxelwise analyses. To visualize the outcome of the statistical test, the significant (i.e., activated) voxels can be displayed on statistical maps of the brain activation using color coding according to the t-score or the p-value for each voxels. The statistical map is usually displayed on anatomical images. In fMRI studies, t-statistic is also commonly used method for ROI-based analysis [18].

1.7.3 Choice of the HRF model

As mentioned in the previous chapter, the shape of the hemodynamic response may differ depending on the specific circumstances, e.g., stimuli, subjects, and the selected brain region. The ability to handle such a variation is controlled by the applied HRF models. In statistical packages for fMRI data analysis, several HRF models are available. A popular approach is to model HRF with a single function with a fixed shape. However, to improve the flexibility of the fitting, HRF can also be modeled as a linear combination of two or more basis functions [19].

The more basis functions involved in the GLM fit, the more flexible the model is in estimating an unexpected HRF shape. However, the increased number of estimated parameters may imply more errors in assessing them. Moreover, it is simpler and statistically more powerful to interpret the results of the estimation on a single parameter than multiple parameters. Because of these problems, a single, rigid model referred to as canonical HRF (CAN) is the most common choice for GLM. The model used in the SPM12 toolbox (Wellcome Trust Centre for Neuroimaging, University College, UK) was defined as a specific combination of two gamma functions. In the case of canonical HRF, only the amplitude of the response is allowed to vary. However, such a rigid model may not assess the shape of the hemodynamic response correctly for much of the brain [20], [11], [21]. Even a small amount of mismodeling can result in a remarkable loss of the statistical power and induces an increase in false positive rate [22], [23].

The use of canonical HRF plus its temporal and dispersion derivatives (Figure 3) can increase the ability to approximate responses that are shifted in time or show different activation duration compared to the canonical HRF [24], [25]. The time derivative allows the onset of the response to change by plus or minus a second, and the dispersion derivative allows a similar amount of variance in the length of the hemodynamic response.

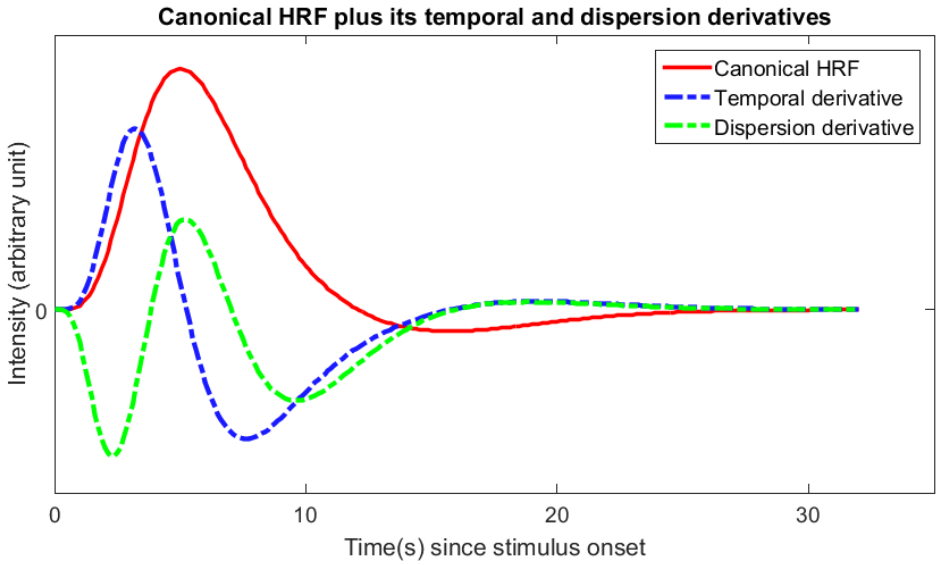

Figure 3. SPM built-in basis functions of canonical HRF plus its temporal and dispersion derivatives.

As another option, the gamma basis functions (Figure 4) are an interesting choice as the canonical HRF is defined as a specific combination of those functions.

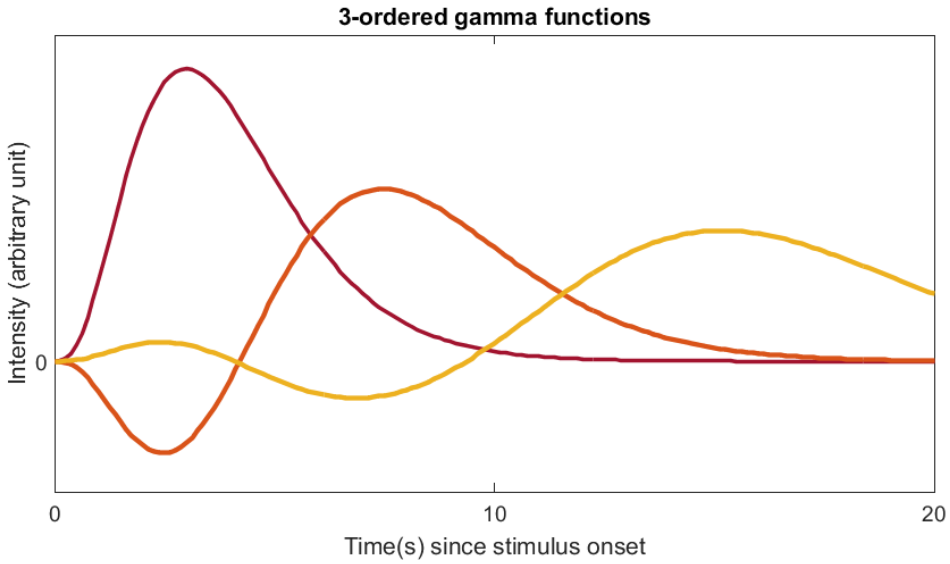

Figure 4. SPM built-in basis functions of 3-ordered gamma functions.

Instead of making an assumption about the shape of the HRF, estimating parameters independently for every timepoint following the stimulus can also be an attractive method. This remarkably flexible approach is called finite impulse response (FIR) model [26]. FIR basis set (Figure 5) consists of a series of n distinct unit-magnitude impulses delayed in time by i *TR, where i = 1, 2, … n. The parameter weight of a given basis function corresponds to the value of the hemodynamic response at the given time point. Unlike previously mentioned models, FIR makes no assumption about the shape of the HRF, all parameter weights can take any value. Thus, FIR is able to estimate a wide range of HRF shapes.

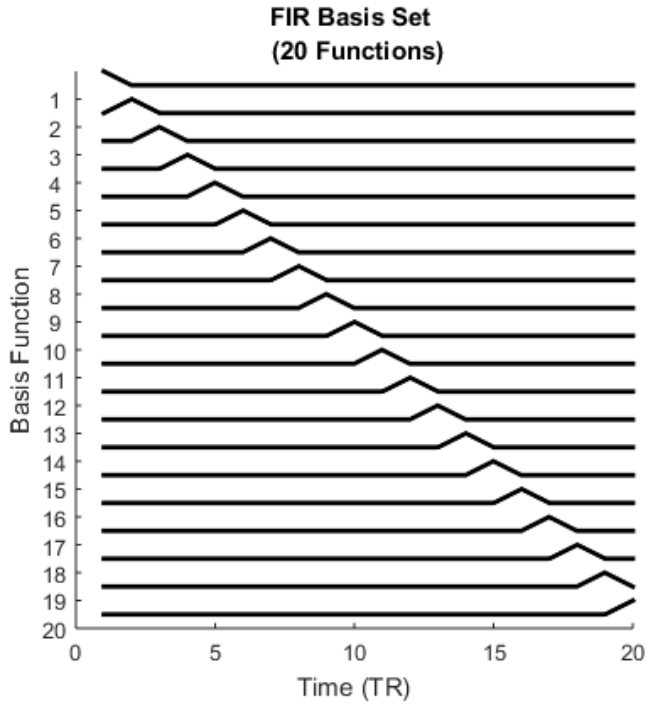

Figure 5. FIR basis set involving 20 basis functions. The basis functions correspond to unit impulses delayed in time by t = 1, 2, … 20 TRs (adapted from [27]).

1.8 The Goodness of Fit measures

Similar to other statistical methods, GLM analyses are controlled by the particular choice of the model [16 - 17]; thus, the quality of the applied model can have a considerable impact on the sensitivity and specificity of statistical tests [18 – 19]. However, the assessment of the model quality has not become a standard practice in the application of GLMs for fMRI. A recently published SPM12 toolbox has been aimed to provide a new package for model assessment, comparison to control model quality and selection termed MACS [25].

Calculation of goodness of fit parameters is a relatively simple approach to quantify the model quality (i.e. how well a model describes a given fMRI signal). The measure aims to determine how well a given model explains the variations in the dataset in question. A regularly applied tool for assessing the goodness of fit of the model is the coefficient of determination (R^2) [22]. R^2 is defined as the ratio of the magnitude of signal variance explained by the model to the magnitude of the total observed signal variance:

$$R^2 = \frac{ESS}{TSS} = 1 - \frac{RSS}{TSS} \tag{4}$$

where RSS is the residual of sum of squares $\sum_{i=1}^{n}(y_i - \hat{y}_i)^2$, ESS is the explained sum of squares $\sum_{i=1}^{n}(\hat{y}_i - \bar{y})^2$ and TSS is the total sum of squares $\sum_{i=1}^{n}(y_i - \bar{y})^2$, such that TSS=RSS+ESS, y_i is the i-th data point in the measured time course, $\hat{y}_i$ is the predicted data (i.e. fitted BOLD signal) for the i-th data point, $\bar{y}$ is the mean signal of the time course, n is the number of data points. In general, the nearer R^2 is to 1, the better the model describes the given dataset. However, R^2 does not account for the number of variables (e.g. number of basis functions) involved in the model, thus R^2 always increases when other variables are added into the model. To avoid overfitting and allow for the comparison between different models, improved goodness of fit indicator is available: the adjusted coefficient of determination [22]:

$$R_a^2 = 1 - \frac{RSS/df_r}{TSS/df_t} \tag{5}$$

where the residual degrees of freedom $df_r = n - p$ (p is the number of model factors) and the total degrees of freedom $df_t = n - 1$ are involved to adjust the R^2 for the number of variables contained by the model. Owing to the addition of the penalty term as the model complexity increases, a higher value of adjusted R^2 indicates higher goodness of fit. Whereas the magnitude of R^2 ranges between 0 (no fit) and 1 (perfect fit), the adjusted R^2 can be negative.

CHAPTER 2

Simultaneous Multislice Imaging in fMRI

Functional MRI measurements mostly rely on the conventional 2D gradient-echo EPI sequence with TR in the range of 2 to 3 s. Regarding the slowness of the BOLD signal, there may seem to be no need for higher sampling rate in time. Despite that, acceleration techniques have been in the focus of interest since their appearance in fMRI measurements. The reason lies in the several advantages provided by higher temporal resolution. First of all, faster sampling of BOLD response has a great potential for increasing statistical power [24], as well as improving temporal modeling of brain dynamics measured with fMRI [3]. The higher sampling rate can reduce temporal aliasing of physiological noise [28]–[30] and allow for advanced characterization of hemodynamic responses. In addition, smaller voxel size can also be achieved without increasing the applied TR: higher number of thin slices can be acquired to cover the whole brain without increase in scan time.

Recently, simultaneous multislice (SMS) or multiband imaging technique using multiband excitation has enabled a considerable advancement in accelerating EPI acquisition [31], [32]. SMS technique, based on the simultaneous excitation and acquisition of multiple slices using multiband RF pulses, allows the acceleration of the acquisition along the slice direction [33], [34]. An excellent review [35] provides a comprehensive snapshot of SMS methodology, with emphasis on excitation, reconstruction and applications. The increase of the temporal resolution and thus the scan time reduction is proportional to the number of slices collected at the same time, which is commonly referred to as multiband factor (MB factor) or SMS acceleration factor. Several studies reported that the application of 2D EPI with MB factor 2 to 12 can provide high quality scans providing reduction in scan time for whole brain and increased temporal resolution [3], [4], [36], [37].

However, the benefit of multiband imaging derived from the shortened TR is achieved at the cost of SNR degradation. Unlike parallel imaging, there is no intrinsic SNR reduction, the decrease is only associated with the g–factor noise of the reconstruction and the incomplete longitudinal relaxation at shorter TRs [32].

Several studies have investigated the benefit of multiband imaging in functional MRI. Numerous studies presented that acquiring a higher number of data points using multiband imaging can improve statistical power [3], [38]. Preibisch et al. [39] found that multiband EPI with MB factor 4 leads to a clear increase in sensitivity for resting-state fMRI, but also observed that higher MB factors induced random artifacts. Todd et al. [40] evaluated the performance of multiband protocols with acceleration factors 2, 4, and 6 for task-based fMRI dataset and demonstrated considerable gains in BOLD sensitivity compared to MB factor 1. They also showed that the MB factor for optimal sensitivity depends on the brain region and the reconstruction method. Demetriou et al. [41] performed a comprehensive test of multiband acquisition protocols and found that its statistical benefit depends on various factors, including the nature of the investigation (resting-state vs. task-based), the experimental design, the particular statistical outcome measure, and the type of analysis used.

Although the effect of the multiband techniques on fMRI experiments has been examined from various aspects, the interaction between the use of multiband imaging and the choice of the HRF model has not been evaluated yet. However, the higher sampling rate can also change the sensitivity to the HRF model inaccuracy due to the higher number of samples measured in a single response. In this work, I aim to investigate this problem by performing GLM fit on fMRI dataset acquired with standard EPI sequence with 2-fold in-plane acceleration (GRAPPA) and multiband EPI with two different multiband factors of 4 and 6 applying five frequently used HRF models.

CHAPTER 3

Methods

The utilized dataset was originally acquired for an earlier study [42] aimed to determine the efficiency of SMS sequences with different measurement durations. The design and the acquisition protocol of the experiment enabled the resulting dataset to be involved in this study in accordance with the previously introduced aims. The fMRI measurements were obtained with standard EPI and EPI with two different multiband protocols; the experimental design was event-related, providing high sensitivity to the shape of the HRF. The purpose of this chapter is to discuss further details about the experiment, as well as the preprocessing and data analysis steps employed in this study. All calculations were performed SPM12 toolbox and custom codes running on MATLAB 2015a (The MathWorks Inc., Natick, MA, USA).

3.1 Data acquisition

Twenty-one healthy, right-handed volunteers were involved in this study. The measurements were performed on a 3 T Siemens Magnetom Prisma scanner (Siemens Healthcare GmbH, Erlangen, Germany) equipped with 64-channel receive-only head coil arrays at the Brain Imaging Centre, Research Centre for Natural Sciences, Hungarian Academy of Sciences.

High-resolution T1-weighted 3D MPRAGE anatomical image (TR = 2300 ms, echo time (TE) = 3 ms, flip angle (FA) = 9°, field of view (FOV) = 256 mm, matrix size 1×1×1 mm) and task-based 2D gradient-echo EPI functional scans were acquired during the experiment. The functional measurements consisted of three different protocols: a standard EPI sequence with twofold in-plane GRAPPA acceleration [43], henceforth referred to as MB1 (i.e. without multiband), and two multiband acquisitions using the blipped-CAIPI approach [32]. The applied MB factors were 4 (MB4) and 6 (MB6) with TRs of 1 s and 0.41 s and flip angles of 64°and 45°, respectively. For MB1, TR was 2 s and the flip angle was 79°. The spatial resolution (matrix size = 3x3x3 mm) and the echo time (TE = 30 ms) were common to all functional scans. The sequence parameters of the

functional scans are summarized in Table 1. Both multiband datasets were reconstructed using LeakBlock kernel [44] to reduce interslice leakage artifacts.

However, four volunteers were excluded owing to excessive head motions (n=1) and missing scans (n=3). Thus, the final fMRI sample consisted of 17 participants (age: mean = 21.7, SD= 2.1).

	MB1	**MB4**	**MB6**
TR (ms)	2000	1000	410
TE (ms)	30	30	30
FA (°)	79	64	45
Total scan volumes	336	672	1638

Table 1. Scanning parameters (adapted from [42])

3.2 Task paradigm

As mentioned previously, the applied task paradigm was event-related. The volunteers performed a visual task comprised of viewing images of faces, viewing images of houses and viewing images of bodies. The presented images were grayscale, framed with a circular contour and displayed centrally. The task also included a baseline condition in which the participants gazed at a fixation point.

Each participant underwent three runs acquired with the scanning protocols introduced above (MB1, MB4 and MB6). The order of the runs was counterbalanced and randomized across the original twenty-one subjects. Each image stimulus was presented for 1 s with an intertrial interval of 2, 5 and 7 s in ~1.5 min long task blocks with six of each stimulus type per block. Each run included 5 task blocks separated by 25 s rest periods, as well as additional 30 s rest periods before the first block and after the last block. The presentation order of the stimuli and the intertrial interval length varied were pseudorandomized in each of the blocks. The same stimuli and design were applied for each subject and run.

To define the location of the regions of interest (ROI) involved in the further analyses, additional independent functional localizer scans were also obtained for each participant with acquisition parameters identical to MB1. Details about the experimental design of the functional localizer measurements can be found in [42].

3.3 Preprocessing

I performed standard preprocessing on each functional dataset using SPM12 toolbox. The utilized preprocessing steps were the following: motion correction, normalization, spatial smoothing, high-pass temporal filtering and prewhitening. The applied SPM routines will be introduced in the next paragraphs.

For the motion correction of the functional data, I used the SPM Realign routine. The algorithm carries out a six-parameter rigid body spatial transformation. Rigid body transformation assumes that the shape and the size of the brain do not vary during the experiment. setsTo eliminate the effect of head motion, the algorithm realigns the time-series of brain volumes to a reference image by a combination of three translations (i.e., movement along the x-, y- and z-axes) and three rotations (i.e. the amount of rotation about x-, y- and z-axes). The six parameters per volume were determined by using the least-squares approach. After realignment, the volumes are resliced corresponding to the calculated parameters such that they match the reference volume.

Prior to the normalization step, I performed the coregistration of the anatomical scan with the functional images. For this purpose, I used the SPM Coregister routine using rigid-body model similar to the realign routine.

I applied the SPM Normalise routine for spatial normalization. During the process, the anatomical and the coregistered functional datasets were transformed into MNI space. The algorithm consists of two components. In the first part, the program estimates a nonlinear deformation field that best overlays the template of the MNI space to the individual anatomical image. The result is a set of warps, which can be applied to the anatomy and the functional images to transform them into the reference space. Deformation is calculated individually for every subject. Then the actual writing of the spatially normalized data is executed by the previously estimated deformation.

I smoothed the data with Gaussian filter implemented in SPM Smoothing routine. The full width at half maximum (FWHM) of the applied kernel was 6 mm in all directions. Besides the spatial smoothing, a 128 s high-pass temporal filter was performed on the data.

An additional preprocessing step was also included to remove temporal autocorrelation (i.e., correlation in the error term) in the fMRI time courses. This effect may arise from the low-frequency scanner drift, oscillatory noise of the cardiac pulse and the respiration

and residual movements remaining after imperfect motion correction [45]. The presence of temporal autocorrelation in the signal can increase the likelihood to detect false positives at first level, which can also be expected to propagate to the group-level [46]. Prewhitening is a common approach to reduce this effect by modeling the temporal autocorrelation. However, increasing sampling rate also increases the temporal autocorrelation of the fMRI time series and the utilization of more complex models for prewhitening is required [30], [47]. It has been demonstrated in recent studies that SPM FAST routine provides an enhanced prewhitening for fMRI datasets even acquired with multiband protocols [46], [47]. The algorithm of FAST models temporal correlation with an extended basis set of covariance matrices (for further details see [47]). In this study, I also used the FAST routine implemented in SPM12 to prewhiten the functional datasets.

3.4 GLM and the estimated parameters

In this study, I analyzed the functional datasets in a GLM framework. Five commonly used SPM built-in HRF models were independently fitted to each functional dataset (already detailed in Section 1.7.3):

a. canonical HRF (CAN)
b. canonical HRF plus its temporal derivative (TD)
c. canonical HRF plus its temporal and dispersion derivatives (DD),
d. finite impulse response model (FIR)
e. 3-order gamma functions (GAMMA).

The selection of the investigated HRF models was based on their frequency in fMRI studies, as well as availability in SPM12. It was also essential to choose models providing different flexibility by using different sets of basis functions varying in number and shape.

The more complex the model is (i.e., including more basis functions), the more parameter estimates are yielded through the GLM fit; however, the interpretation of multiple parameters may not be trivial. For simplicity, I performed further statistical analyses using a single parameter as an estimation of the HRF amplitude (H) for each model. These parameters were computed as a combination of the estimated parameters obtained through the GLM fit.

When using canonical HRF, a single parameter is obtained individually for each condition. However, including the derivative terms in the model results in additional

parameter estimates, one for each additional derivative terms. Considering only the non-derivative term may induce amplitude bias due to the delay difference between the model and the measured time series. To counteract these effects, H was calculated by incorporating the derivative terms proposed by [48].

For TD

$$H = sign(\hat{\beta}_1)\sqrt{\hat{\beta}_1{}^2 + \hat{\beta}_2{}^2} \quad (6)$$

where $\hat{\beta}_1$ is the estimated parameters for the canonical HRF and $\hat{\beta}_2$ is for the temporal derivative term.

For DD

$$H = sign(\hat{\beta}_1)\sqrt{\hat{\beta}_1{}^2 + \hat{\beta}_2{}^2 + \hat{\beta}_3{}^2} \quad (7)$$

where $\hat{\beta}_1$ is the estimated parameters for the canonical HRF and $\hat{\beta}_2$ and $\hat{\beta}_3$ is for the temporal and dispersion derivative terms, respectively.

When considering GAMMA, I used the same approach as for the canonical model plus its derivatives to determine H:

$$H = sign(\hat{\beta}_1)\sqrt{\hat{\beta}_1{}^2 + \hat{\beta}_2{}^2 + \hat{\beta}_3{}^2} \quad (8)$$

where $\hat{\beta}_1$, $\hat{\beta}_2$ and $\hat{\beta}_3$ are the estimated parameters for the fitted gamma functions.

For FIR, I calculated the average of the estimated parameters assigned to the interval ranged between 4 and 6 s from the stimulus onset:

$$H = \frac{1}{n}\sum_{i=t}^{t+n}\hat{\beta}_i \quad (9)$$

where n is the number of averaged estimated parameters ($n = \frac{2}{TR} + 1$), t is the index of the basis function corresponding to 4 s from the stimulus onset and $\hat{\beta}_i$ is the estimated parameter for the ith basis function of the FIR model. The investigated interval for averaging was defined based on the individual HRF estimations using FIR considering each subject and MB factor to include a period around the peak.

3.5 Identification of ROIs

Four object-selective visual cortical regions were defined based on anatomical landmarks and statistical contrast maps (thresholded at $p < 0.001$, uncorrected) individually using the functional localizer scans:

- fusiform face area (FFA) responding more intensely when the subjects viewed faces than when they viewed other categories of objects [49]
- occipital face area (OFA) also responding selectively to faces [50]
- parahippocampal place area (PPA) responding selectively to passively viewed scenes and houses [51]
- extrastriate body area (EBA) responding selectively to human body [52]

The statistical contrast maps were created based on GLM approach using canonical HRF.

The fusiform face area (FFA) and the occipital face area (OFA) were determined as the areas responding more intensely to faces relative to houses. The parahippocampal place area (PPA) was identified as the area showing higher activation magnitude to houses than faces. Both right and left FFA were defined in 14 subjects, whereas right and left OFA were identified in 14 and 13 subjects, respectively. The right and left PPA and right and left EBA were found in all subjects. The locations of the ROIs are displayed in Figure 6.

The investigated volumes for the ROI-based analyses were defined as a sphere with radius of 6 mm and centrally located around the peak voxel of the identified ROI. On the extracted sphere volumes, individually determined (using SPM Segmentation routine) gray matter mask was also applied. The locations of the investigated volumes are represented in Figure 6.

3.6 Outcome metrics

I investigated the interaction between the higher sampling rate acquired with multiband imaging and the choice of the HRF model from two aspects. Firstly, I approached this problem by testing the combined effect of these factors on statistical outcome measures of the image stimuli (face, house and body) vs. baseline contrast at both subject-level and group-level. Secondly, to examine the influence of higher temporal sampling obtained with the multiband imaging on the performance of the different HRFs, I carried out GoF measures of the GLM fit. The applied calculations are discussed in the following sections.

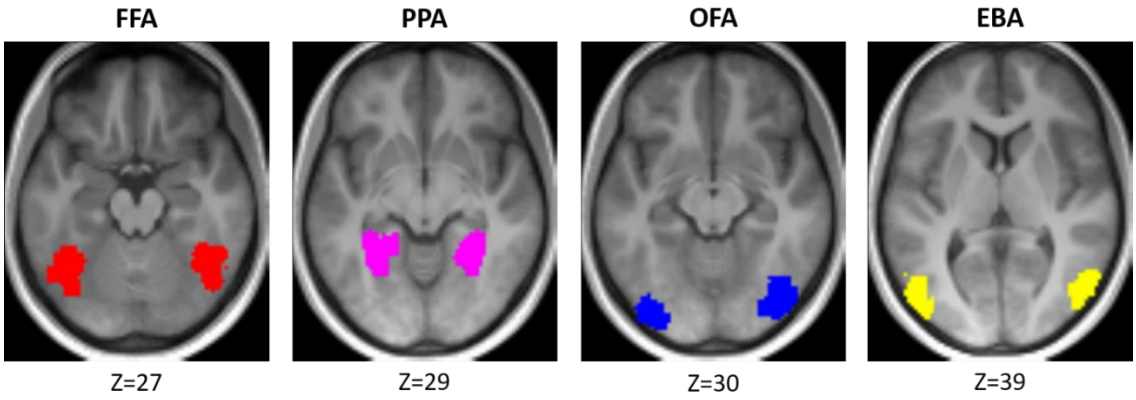

Figure 6. Locations of the investigated ROIs based on the union of the individual ROIs. The clusters are overlaying on a group-average anatomical image. The z coordinates of the axial slices are MNI coordinates (Abbreviations: FFA= fusiform face area, OFA = occipital face area, PPA = parahippocampal place area, EBA = extrastriate body area).

3.6.1 Group-level statistics

Group-level random-effects analyses were performed on individual H values (introduced in Section 3.4) voxel by voxel for each dataset and model. H values were averaged across image stimuli (face, house, and body) to investigate all image stimuli versus baseline contrast in the voxelwise analysis. The resulted t-score maps were thresholded at $p<0.001$ (uncorrected) and masked by SPM built-in grey matter mask. Furthermore, the number of grey matter voxels exceeding the threshold were also extracted.

Group-level t-statistics were conducted on ROI-averaged H values for each model - MB factor combination as well. The input values were computed by calculating a simple mean of the H values within each ROI, then averaging it across hemispheres for each subject. Contrary to voxelwise analysis, the contrasts were chosen to compare that image stimulus the specific area is selective for with the baseline: face versus baseline for FFA and OFA, house versus baseline for PPA and body versus baseline for EBA.

3.6.2 Subject-level statistics

For subject-level investigations, voxelwise t-scores were obtained for a representative subject in case of each MB factor - HRF model combination. However, the resulted t-scores can not be directly compared at subject-level due to the different degrees of freedom arising from the different number of observations and estimated parameters. Even the same t-scores can mean different statistical significance and produce different outputs (e.g. in assessing whether a voxel is active or not). Thus, voxelwise p-values (i.e. whole-brain probability maps) were calculated based on the resulted t-scores for the representative subject in case of each MB factor - HRF model combination. The number of grey matter voxels were also obtained exceeding threshold $p = 0.001$ (uncorrected).

3.6.3 Goodness of Fit measures

As mentioned previously, the quality of the GLM fit using different models was characterized via GoF measures. I calculated voxelwise adjusted R^2 using the SPM MACS toolbox resulting in whole-brain maps for each subject and HRF model-MB factor combination. On the resulted individual maps, both whole-brain and ROI-based analyses were carried out.

Group-level mean maps were produced by averaging the individual adjusted R^2 maps for each MB factor-HRF model combination. In addition, group-level across-model mean maps were obtained for each fMRI dataset.

Furthermore, I calculated the group-level means of ROI-averaged adjusted R^2 values for each MB factor-HRF model combination within each ROI. The individual ROI-averaged adjusted R^2 values were computed identically to the individual ROI-averaged H values described in Section 3.6.1.

To determine the effects of the scanning protocol and the HRF model or if there is any interaction between them, I performed two-way repeated measures analysis of variance (ANOVA) with factors MB factor (MB1, MB4, MB6) and HRF model (CAN, TD, DD, FIR, GAMMA) on the ROI-averaged R^2 values. Mauchly's test of sphericity [53] indicated that the assumption of sphericity had been violated ($p<0.05$), thus Greenhouse-Geisser correction [54] was applied on the results of two-way repeated measures ANOVA.

To obtain detailed information on the pairwise differences between specific groups, multiple comparison analysis was also conducted using Tukey's Honestly Significant Difference Procedure for each ROI. This method involves correction for multiple comparisons to avoid incorrect rejection of the null hypothesis owing to the large number of tests. Significance was set at $p < 0.05$. Two-way repeated measures ANOVA, Mauchly's test and multiple comparison analysis was performed using MATLAB built-in functions.

CHAPTER 4

Results

4.1 Goodness of Fit measures

In Figure 7, the same axial slices of the group-level mean adjusted R^2 maps are shown for the three MB factors and the five HRF models. The images show an apparent decrease in GoF values for MB6, while the MB4 provides a similar level of adjusted R^2 values compared to MB1. The sign of the differences between MB1 and MB4 shows high region dependence for all models.

For each MB factor, a similar trend of GoF is seen across models, TD and DD had the highest and GAMMA had the lowest adjusted R^2 values. Despite its high flexibility, FIR did nor provide the best fit. Figure 7 and Figure 8 show a similar spatial pattern with superior adjusted R^2 values seen in the visual cortex, the differences between MB6 and the other two scanning protocols also peaks in the visual cortex.

The ROI-based analysis supported these results. (Figure 9). A clear drop is seen in GoF measures at MB6 compared to MB1 and MB4 for all regions and HRF models. Furthermore, similar across-model trends were observed in the investigated ROIs with higher GoF for TD, DD and FIR and lower for CAN and GAMMA. Similar to the whole-brain analysis, the use of GAMMA produced the lowest GoF measures. The differences amongst the models showed a pronounced reduction for MB6 compared to MB4 and MB1. PPA, located in a brain area characterized by reduced SNR due to severe distortion and signal loss [55], provided a lower GoF compared to the other three ROIs, with mean adjusted R^2 values below 0.09.

In all the four ROIs, the two-way repeated-measures ANOVA with Greenhouse-Geisser correction indicated significant differences in adjusted R^2 values related to either MB factor (FFA: $F(1.95,29.32) = 10.47$, $p<0.001$; OFA : $F(1.95,25.36) = 15.33$, $p<0.001$; PPA: $F(1.89,30.20) = 22.04$, $p<0.001$, EBA: $F(1.88,30.01)=12.26$, $p<0.001$) or HRF model (FFA: $F(3.77,56.59) = 36.69$, $p<0.001$; OFA : $F(3.73,48.45) = 51.94$, $p<0.001$; PPA: $F(3.01,48.12) = 26,61$, $p<0.001$, EBA: $F(3.58,57.23) = 32.38$, $p<0.001$).

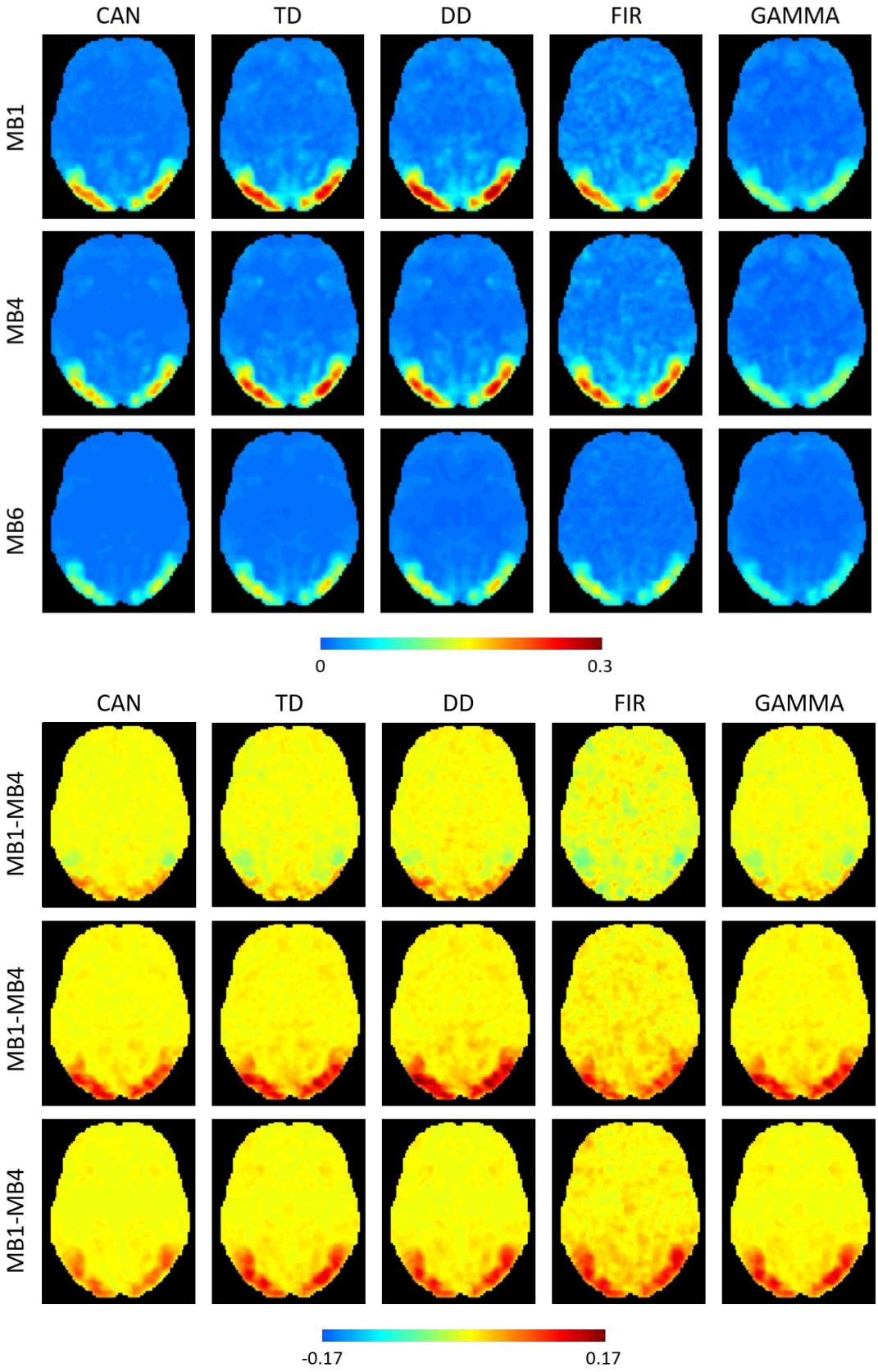

Figure 7. Maps of group-level mean R^2 values for each MB factor and HRF model (upper panel) and differences considering MB factor (lower panel). The images present the same axial slice (z=36, MNI coordinate).

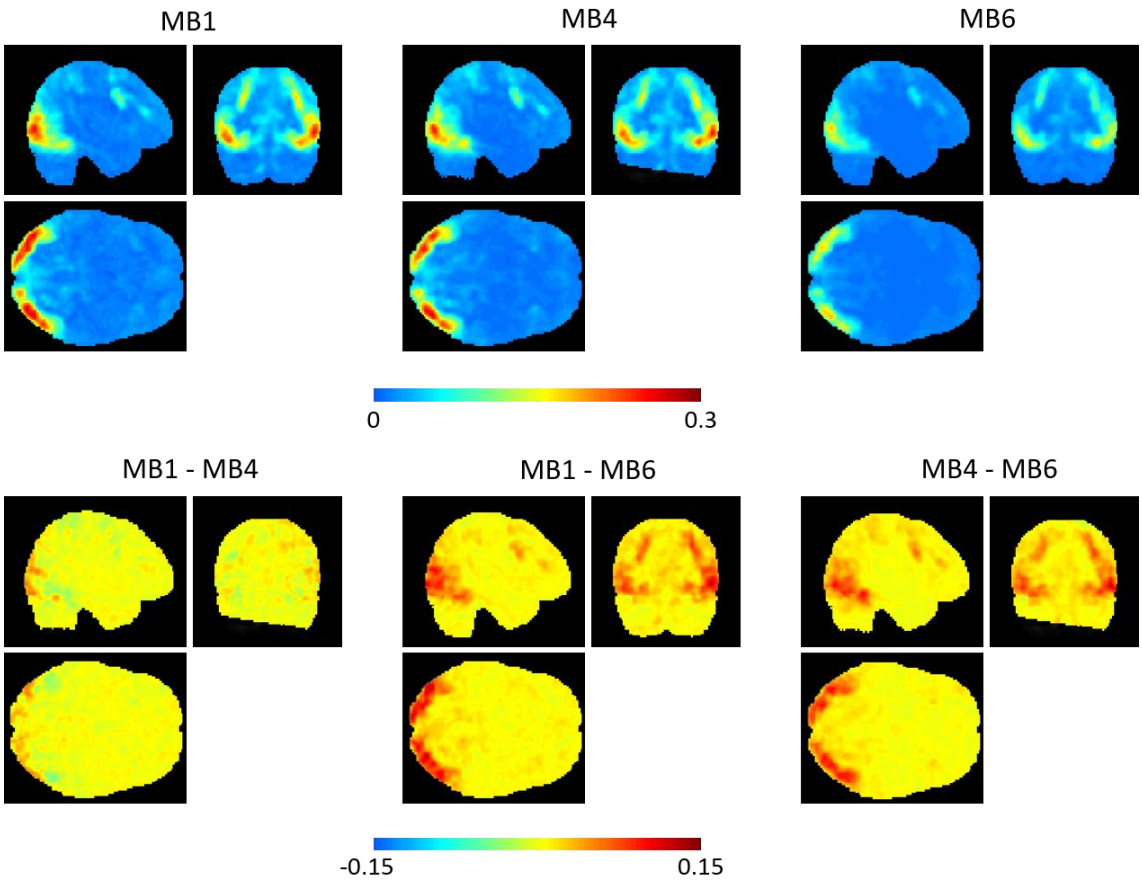

Figure 8. Maps of across-model group-level mean of adjusted R^2 values and differences between them. The images present the same axial, coronal and sagittal slices (MNI coordinates: x = 60, y = 20, z = 36).

Furthermore, there was a significant interaction between MB factor and HRF model (FFA: $F(1.55,23.3) = 6.74$, $p<0.001$; OFA: $F(1.81,23.55) = 6.51$, $p<0.001$; PPA: $F(1.48,23.65) = 8.78$, $p<0.001$, EBA: $F(1.71,27.35) = 5.85$, $p<0.001$), which means that the GoF of a specific model depends on the utilized MB factor the fMRI dataset were acquired with.

The results of multiple comparison analyses can be found in the Appendix (Tables A1-A8). The multiple comparisons revealed a significant reduction in GoF for MB6 compared to MB1 and MB4 in most cases (Tables A1-A4). Though Figure 9 shows small differences between the mean adjusted R^2 values of MB1 and MB4, the pairwise comparisons indicated no significant differences for all HRF models and ROIs, with the exception of a few cases in OFA (Table A2). As seen in Figure 9, the across-model differences at MB6 are smaller compared to MB1 and MB4, in FFA, only one across-model comparison was significant at MB6: FIR vs. DD (Table A5). Considering the models with the highest R^2 mean values, TD, DD and FIR differ significantly in most

cases at MB1 and MB6, however, indicates no significant differences at MB4 in each region (Table A5-A8). It is also noteworthy that compared to the most frequently used model CAN, the more flexible models as TD, DD and FIR do not always provide better GoF depending on the investigated brain region and the acquisition protocol.

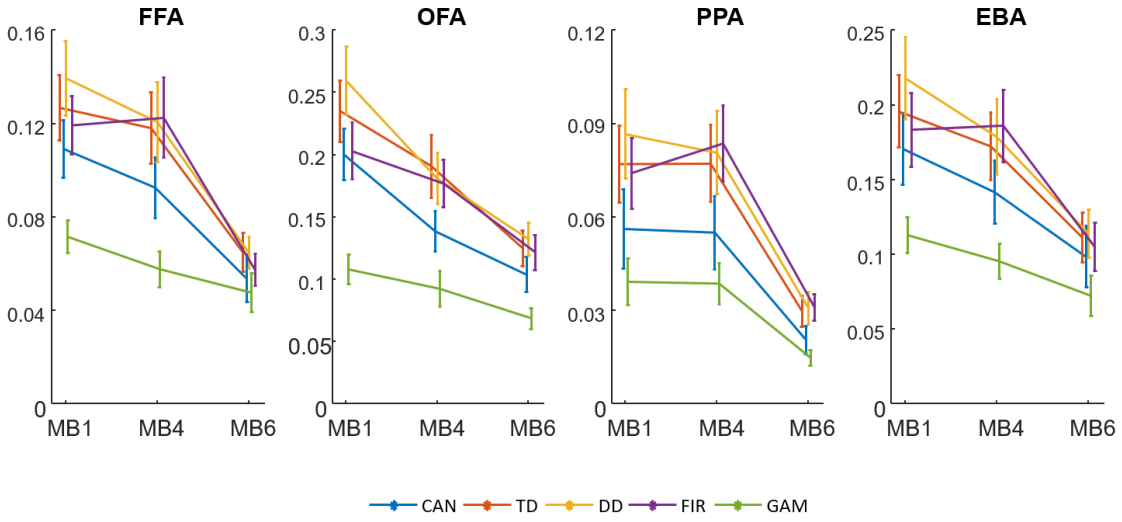

Figure 9. Group-level means of ROI-averaged adjusted R^2 values for each MB factor and HRF models with their standard error in each ROI. The individual plots are scattered around MB1, MB4, and MB6 horizontally only for visualization purposes.

4.2 Group-level statistics

Figure 10 shows axial slices of the group-level t-score maps thresholded at $p<0.001$ (uncorrected), displaying voxels identified as active, resulted in the random effect analysis for each dataset and model. The same axial slice is represented as for Figure 7. The spatial pattern and the intensity of the identified activations indicate a high dependency on the choice of the model and the MB factor. The visual cortex is displayed as active in all images, however, the intensity and the spatial extent vary amongst models and MB factors (e.g., active regions for MB4-GAMMA are more extended than MB6-FIR). Furthermore, Figure 10 shows that MB4 and MB6 reveal additional regions as active: significant voxels with peak activation located in the parahippocampal gyrus and in insula (denoted by green and yellow arrays in Figure 10, respectively), which are not detected or containing only a few voxels when using MB1. The extent and the intensity in these regions also show high model-specific dependence, e.g. FIR and DD detected fewer voxels in insula compared to the other models.

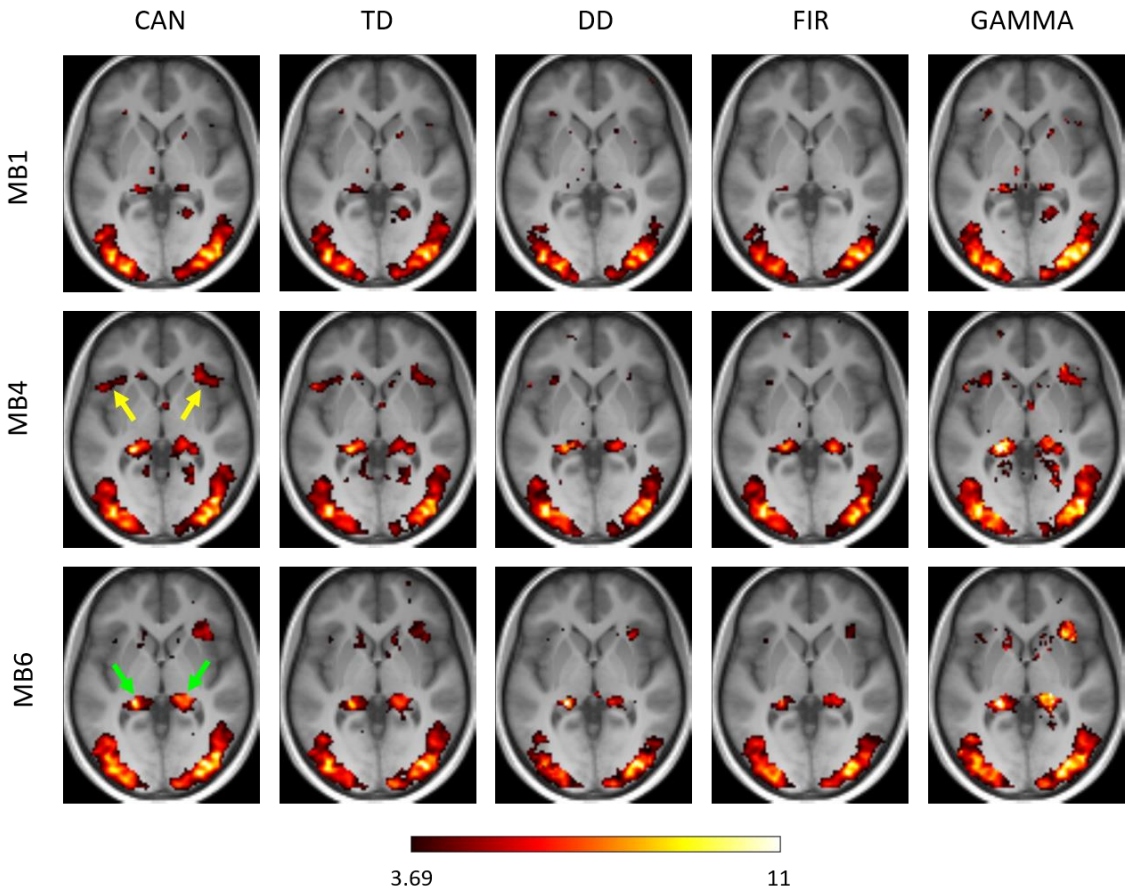

Figure 10. Group-level t-score maps for each MB factor and HRF model. Each map is thresholded at T=3.69 ($p<0.001$, uncorrected). The t-scores are overlaid on a group-average anatomical image presenting the same axial slice (z = 36, MNI coordinate). Green and yellow arrows denote active voxels in the insula and the parahippocampal cortex, respectively.

The extracted numbers of activated voxels are shown in Figure 11. The results revealed a similar across-model trend for all acquisition protocol, CAN, TD and GAMMA provided the highest, FIR and DD provided the lowest values. MB4 produced the highest number of activated voxels for each model. The average number of activated voxels was slightly larger at MB6 compared to MB1. The across-model variability measured by CV reveals a clear increase with MB factor.

The results of the ROI-based group-level t-statistics (Figure 12) show a crucial dependence on region, MB factor and HRF model. The highest t-scores are seen at MB6 in 13 of the total 20 cases. MB1 appears to outperform MB6 and MB4 only in one case, fitting GAMMA within EBA. In the case of CAN, MB6 provided higher t-scores compared to MB1 and MB4 within each ROI. Looking at the results of other models, no apparent MB factor superiority can be observed.

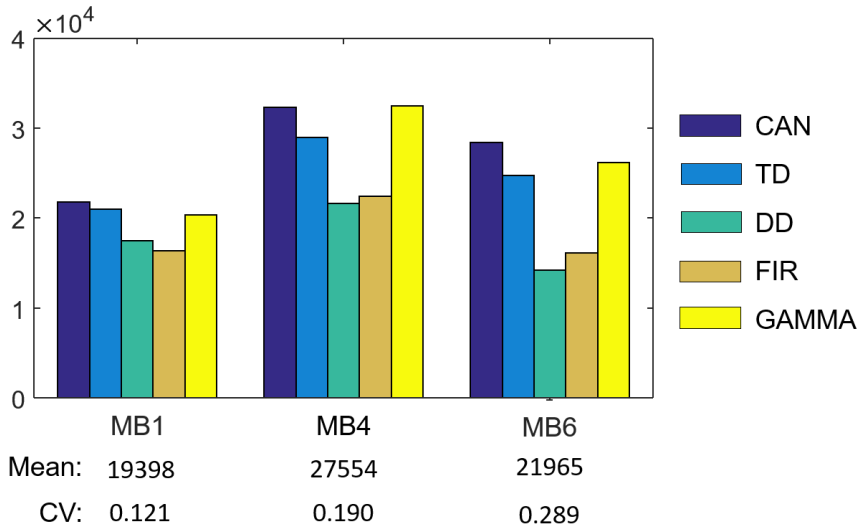

Figure 11. The number of activated voxels within SPM built-in grey-matter mask extracted from group-level t-maps thresholded at T=3.69 ($p<0.001$) for each HRF model and MB factor. The across-model means (Mean) and the coefficient of variation (CV) are also displayed.

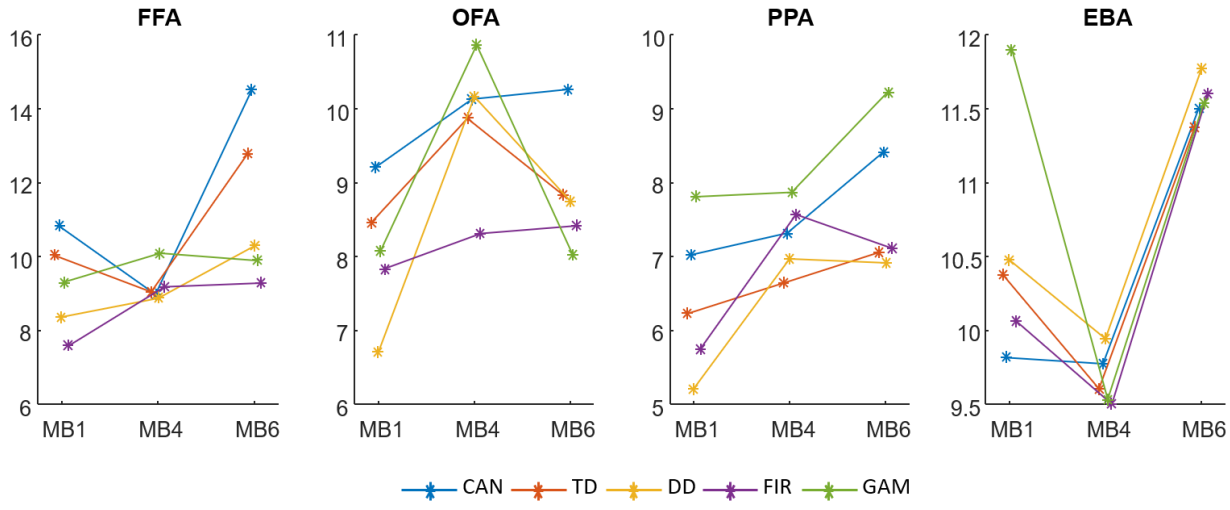

Figure 12. ROI-based group-level t-scores for each MB factor and HRF model.

4.3 Subject-level statistics

Figure 13 shows axial slices of the subject-level probability maps thresholded at p<0.001 (uncorrected), displaying voxels labeled as active. The images show somewhat similar results as with the group-level t-maps (Figure 10): high dependency on the choice of the model and the MB factor can be observed. Furthermore, the application of MB4 and MB6 also produces additional active areas or reveals detected regions with expanded spatial extent when compared with MB1 (e.g. in insula and parahippocampal gyrus). The acquired number of activated voxels (Figure 14) also confirmed that: the across-model mean was the highest for MB4 and the second-highest for MB6. However, the acquired coefficient of variation values indicate lower across-model variability for multiband protocols (MB4 and MB6) compared to MB1 in the case of the representative subject disagreeing with the group-level results.

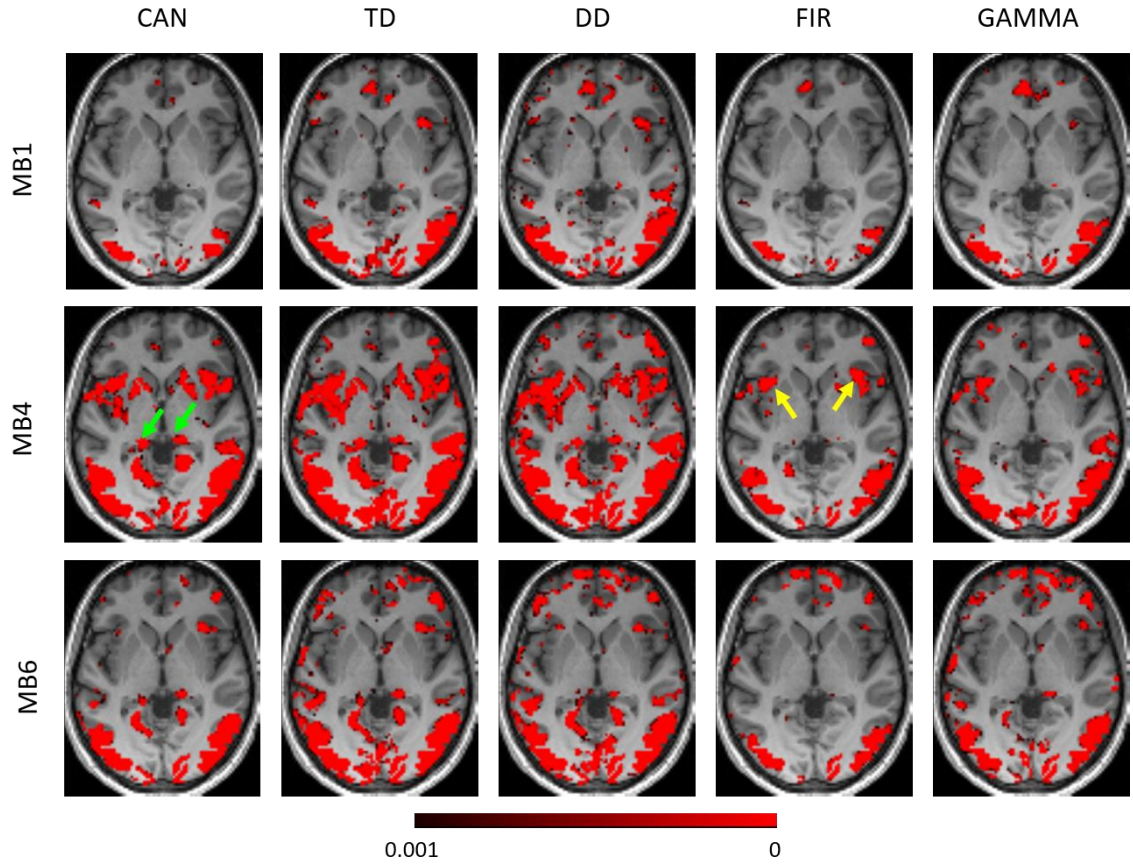

Figure 13. Probability maps thresholded at p<0.001 (uncorrected) from a representative subject for each MB factor and HRF model. The p-values are overlaid on the individual anatomical image (after transformation into MNI space) presenting the same axial slice (z = 36, MNI coordinate). Only voxels within individual grey matter mask are displayed. Green and yellow arrows denote active voxels in the insula and the parahippocampal cortex, respectively.

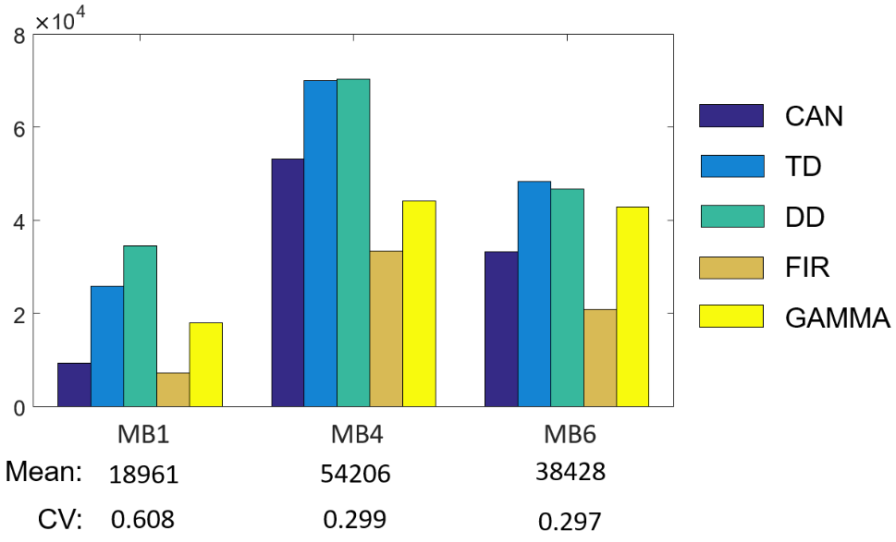

Figure 14. The number of activated voxels within the individual grey-matter mask extracted from subject-level probability maps thresholded at p<0.001(uncorrected) for each HRF model and MB factor. The values were obtained for a representative subject. The across-model means (Mean) and the coefficient of variation (CV) are also displayed.

CHAPTER 5

Discussion and conclusion

The interaction between acceleration using multiband protocols and applied HRF model has been investigated by evaluating three different scanning protocols (standard EPI with 2-fold in-plane acceleration (GRAPPA) without multiband: MB1, MB4 and MB6) and five SPM built-in HRF models. For this purpose, statistical analysis was performed on both group-level and subject-level. Furthermore, adjusted R^2 values were calculated to estimate the quality of the GLM fit using different models.

The multiband protocols showed possible benefits in t-statistics at both group-level and subject-level using the examined models. Based on the statistical maps (t-scores at group-level and p-values at subject-level), additional areas were identified as active which may be relevant to the task: significant voxels with peak activation located in the posterior part of the parahippocampal gyrus and in the anterior insula were observed. The posterior part of the parahippocampal gyrus plays an essential role in visual processing [56], [57], the anterior insula as a part of the saliency network subserves high-level cognitive control and attentional mechanisms facilitating task-related information processing [58], [59]. The extent and the intensity of these activations also show apparent across-model variance for each MB factor. The assessment of the number of activated voxels revealed higher across-model mean for the multiband protocols at both group-level and subject-level. Furthermore, the increased across-model variability in number of activated voxels for MB4 and MB6 indicates that the use of the multiband techniques may increase the sensitivity to the HRF models at group-level. However, the results from a representative subject have not confirmed that at subject-level.

Furthermore, considering ROI-based analysis, multiband protocols also indicate gains on t-statistics at group-level in the majority of the investigated MB factor-HRF model combinations. However, it is noteworthy that the increased number of activations and t-scores may result from task-independent effects, e.g. the incomplete correction of the interslice leakage and the increased temporal autocorrelation owing to multiband acquisition. However, even when MB6 protocols produced increased t-scores at group-level, GoF measures indicated a significant reduction for this dataset compared to MB1

and MB4, which also challenge the reliability of the datasets acquired with higher MB factor. This effect may be due to the SNR loss related to g-factor penalty of the multiband technique, the incomplete T1 relaxation and the inaccuracy of the applied models. The degree of contributions of these factors is not clear.

The results make no clear suggestion which investigated acquisition protocol and model should be used when conducting task-based fMRI experiment, statistical benefit at group level as well as higher across-model sensitivity may come from the higher sampling rate obtained with multiband techniques. However, the quality of the GLM fit may also decrease. Considering the revealed spatial variability, one should take into account the investigated brain region when choosing multiband acceleration and HRF model for the GLM fit.

CHAPTER 6

Summary

Accurate modeling of the hemodynamic response function (HRF) is still of great interest in functional MRI (fMRI) research. The emergence of multiband techniques has enabled temporal sampling rates to be significantly higher, which can also change the sensitivity to the HRF model misspecification due to the higher number of samples obtained in a single response. The aim of the current thesis was to investigate the interaction between the use of multiband techniques and the choice of the HRF model in General Linear Model (GLM) fit.

For this purpose, I evaluated fMRI datasets obtained with standard EPI sequence with 2-fold in-plane GRAPPA acceleration (MB1) and multiband EPI with two different multiband factors, 4 (MB4) and 6 (MB6). After carrying out standard preprocessing steps, I analyzed the functional datasets in a GLM framework. Five commonly used SPM built-in HRF models were independently fitted to each functional dataset.

Based on the parameters obtained with GLM fit, I computed voxelwise statistical outcome measures at both subject-level and group-level. To estimate the quality of the GLM fit using different models, I calculated adjusted coefficient of determination (R^2) values as a goodness of fit (GoF) measures. Region of interest (ROI) analyses were also performed for group-level statistics and GoF measures using four object-selective brain regions.

The results show significant interaction between the choice of the HRF model and the applied MB factor for each outcome measure. Both group-level and subject-level statistical maps indicated that the use of multiband protocols could reveal additional, potentially relevant active areas (e.g. in insula) compared to MB1, also confirmed by the higher mean number of activated voxels. The extent of the activations shows high across-model variance for each investigated acquisition protocol.

Furthermore, considering ROI-based analysis, multiband protocols also indicate gains on t-statistics at group-level in the majority of the investigated MB factor-HRF model combinations. However, even when MB6 protocols produced increased t-scores at group-level, GoF measures indicated a significant reduction for this dataset compared to MB1

and MB4. This effect may be due to the SNR loss related to g-factor penalty of the multiband technique, the incomplete T1 relaxation and the inaccuracy of the applied models.

The results also show substantial region-dependency of the outcome measures using different MB factor-HRF model combinations. Therefore, when considering multiband protocol and the HRF model, one should also take into account the investigated brain region.

References

[1] G. H. Glover, “Overview of Functional Magnetic Resonance Imaging,” *Neurosurgery Clinics*, vol. 22, no. 2, pp. 133–139, Apr. 2011, doi: 10.1016/j.nec.2010.11.001.

[2] P. Jezzard, P. M. Matthews, and S. M. Smith, Eds., *Functional MRI: An Introduction to Methods*, 1 edition. Oxford: Oxford University Press, 2002.

[3] D. A. Feinberg *et al.*, “Multiplexed echo planar imaging for sub-second whole brain FMRI and fast diffusion imaging,” *PloS one*, vol. 5, no. 12, 2010.

[4] D. A. Feinberg and K. Setsompop, “Ultra-fast MRI of the human brain with simultaneous multi-slice imaging,” *Journal of magnetic resonance*, vol. 229, pp. 90–100, 2013.

[5] S. Ogawa, T. M. Lee, A. R. Kay, and D. W. Tank, “Brain magnetic resonance imaging with contrast dependent on blood oxygenation.,” *Proceedings of the National Academy of Sciences*, vol. 87, no. 24, pp. 9868–9872, Dec. 1990, doi: 10.1073/pnas.87.24.9868.

[6] K. K. Kwong *et al.*, “Dynamic magnetic resonance imaging of human brain activity during primary sensory stimulation.,” *Proceedings of the National Academy of Sciences*, vol. 89, no. 12, pp. 5675–5679, Jun. 1992, doi: 10.1073/pnas.89.12.5675.

[7] S. Ogawa *et al.*, “Intrinsic signal changes accompanying sensory stimulation: functional brain mapping with magnetic resonance imaging.,” *Proceedings of the National Academy of Sciences*, vol. 89, no. 13, pp. 5951–5955, Jul. 1992, doi: 10.1073/pnas.89.13.5951.

[8] L. Pauling and C. D. Coryell, “The Magnetic Properties and Structure of Hemoglobin, Oxyhemoglobin and Carbonmonoxyhemoglobin,” *Proc Natl Acad Sci USA*, vol. 22, no. 4, pp. 210–216, Apr. 1936, doi: 10.1073/pnas.22.4.210.

[9] K. R. Thulborn, J. C. Waterton, P. M. Matthews, and G. K. Radda, “Oxygenation dependence of the transverse relaxation time of water protons in whole blood at high field,” *Biochimica et Biophysica Acta (BBA) - General Subjects*, vol. 714, no. 2, pp. 265–270, 0 1982, doi: 10.1016/0304-4165(82)90333-6.

[10] S. A. Huettel, A. W. Song, and G. McCarthy, *Functional Magnetic Resonance Imaging*. Sinauer Associates, 2004.

[11] D. A. Handwerker, J. M. Ollinger, and M. D’Esposito, “Variation of BOLD hemodynamic responses across subjects and brain regions and their effects on statistical analyses,” *Neuroimage*, vol. 21, no. 4, pp. 1639–1651, 2004.

[12] E. A. Disbrow, D. A. Slutsky, T. P. Roberts, and L. A. Krubitzer, “Functional MRI at 1.5 tesla: a comparison of the blood oxygenation level-dependent signal and electrophysiology,” *Proceedings of the National Academy of Sciences*, vol. 97, no. 17, pp. 9718–9723, 2000.

[13] N. K. Logothetis, J. Pauls, M. Augath, T. Trinath, and A. Oeltermann, “Neurophysiological investigation of the basis of the fMRI signal,” *Nature*, vol. 412, no. 6843, pp. 150–157, 2001.

[14] D. A. Feinberg, A. T. Vu, and A. Beckett, “Pushing the limits of ultra-high resolution human brain imaging with SMS-EPI demonstrated for columnar level fMRI,” *Neuroimage*, vol. 164, pp. 155–163, 2018.

[15] P. Mansfield, “Multi-planar image formation using NMR spin echoes,” *Journal of Physics C: Solid State Physics*, vol. 10, no. 3, p. L55, 1977.

[16] S. A. Huettel, “Event-related fMRI in cognition,” *NeuroImage*, vol. 62, no. 2, pp. 1152–1156, 0 2012, doi: 10.1016/j.neuroimage.2011.08.113.

[17] M. Brett, I. S. Johnsrude, and A. M. Owen, “The problem of functional localization in the human brain,” *Nature Reviews Neuroscience*, vol. 3, no. 3, pp. 243–249, Mar. 2002, doi: 10.1038/nrn756.

[18] R. A. Poldrack, “Region of interest analysis for fMRI,” *Social cognitive and affective neuroscience*, vol. 2, no. 1, pp. 67–70, 2007.

[19] K. J. Friston, P. Fletcher, O. Josephs, A. Holmes, M. D. Rugg, and R. Turner, “Event-related fMRI: characterizing differential responses,” *Neuroimage*, vol. 7, no. 1, pp. 30–40, 1998.
[20] R. M. Birn, Z. S. Saad, and P. A. Bandettini, “Spatial heterogeneity of the nonlinear dynamics in the FMRI BOLD response,” *Neuroimage*, vol. 14, no. 4, pp. 817–826, 2001.
[21] T. D. Wager, A. Vazquez, L. Hernandez, and D. C. Noll, “Accounting for nonlinear BOLD effects in fMRI: parameter estimates and a model for prediction in rapid event-related studies,” *NeuroImage*, vol. 25, no. 1, pp. 206–218, 2005.
[22] M. Razavi *et al.*, “Model assessment and model building in fMRI,” *Human brain mapping*, vol. 20, no. 4, pp. 227–238, 2003.
[23] M. M. Monti, “Statistical analysis of fMRI time-series: a critical review of the GLM approach,” *Frontiers in human neuroscience*, vol. 5, p. 28, 2011.
[24] R. T. Constable and D. D. Spencer, “Repetition time in echo planar functional MRI,” *Magnetic Resonance in Medicine: An Official Journal of the International Society for Magnetic Resonance in Medicine*, vol. 46, no. 4, pp. 748–755, 2001.
[25] J. Soch and C. Allefeld, “MACS–a new SPM toolbox for model assessment, comparison and selection,” *Journal of neuroscience methods*, vol. 306, pp. 19–31, 2018.
[26] G. H. Glover, “Deconvolution of impulse response in event-related BOLD fMRI1,” *Neuroimage*, vol. 9, no. 4, pp. 416–429, 1999.
[27] “fMRI in Neuroscience: Modeling the HRF With FIR Basis Functions,” *The Clever Machine*, Dec. 17, 2012. https://theclevermachine.wordpress.com/2012/12/16/fmri-in-neuroscience-modeling-the-hrf-with-fir-basis-functions/ (accessed May 22, 2020).
[28] L. R. Frank, R. B. Buxton, and E. C. Wong, “Estimation of respiration-induced noise fluctuations from undersampled multislice fMRI data,” *Magnetic Resonance in Medicine: An Official Journal of the International Society for Magnetic Resonance in Medicine*, vol. 45, no. 4, pp. 635–644, 2001.
[29] Y. Tong, L. M. Hocke, and B. deB Frederick, “Short repetition time multiband echo-planar imaging with simultaneous pulse recording allows dynamic imaging of the cardiac pulsation signal,” *Magnetic resonance in medicine*, vol. 72, no. 5, pp. 1268–1276, 2014.
[30] A. K. Sahib *et al.*, “Effect of temporal resolution and serial autocorrelations in event-related functional MRI,” *Magnetic resonance in medicine*, vol. 76, no. 6, pp. 1805–1813, 2016.
[31] R. G. Nunes, J. V. Hajnal, X. Golay, and D. J. Larkman, “Simultaneous slice excitation and reconstruction for single shot EPI,” in *Proc Intl Soc Mag Reson Med*, 2006, vol. 14, no. 2, p. 293.
[32] K. Setsompop, B. A. Gagoski, J. R. Polimeni, T. Witzel, V. J. Wedeen, and L. L. Wald, “Blipped-controlled aliasing in parallel imaging for simultaneous multislice echo planar imaging with reduced g-factor penalty,” *Magnetic resonance in medicine*, vol. 67, no. 5, pp. 1210–1224, 2012.
[33] A. Maudsley, “Multiple Line Scanning Spin Density Imaging,” *Journal of Computer Assisted Tomography*, vol. 5, no. 2, pp. 289–290, 1981.
[34] S. Müller, “Multifrequency selective RF pulses for multislice MR imaging,” *Magnetic resonance in medicine*, vol. 6, no. 3, pp. 364–371, 1988.
[35] M. Barth, F. Breuer, P. J. Koopmans, D. G. Norris, and B. A. Poser, “Simultaneous multislice (SMS) imaging techniques,” *Magnetic resonance in medicine*, vol. 75, no. 1, pp. 63–81, 2016.
[36] J. Xu *et al.*, “Evaluation of slice accelerations using multiband echo planar imaging at 3 T,” *Neuroimage*, vol. 83, pp. 991–1001, 2013.
[37] K. Uğurbil *et al.*, “Pushing spatial and temporal resolution for functional and diffusion MRI in the Human Connectome Project,” *Neuroimage*, vol. 80, pp. 80–104, 2013.
[38] S. M. Smith *et al.*, “Resting-state fMRI in the human connectome project,” *Neuroimage*, vol. 80, pp. 144–168, 2013.

[39] C. Preibisch, M. Bührer, and V. Riedl, “Evaluation of multiband EPI acquisitions for resting state fMRI,” *PloS one*, vol. 10, no. 9, p. e0136961, 2015.
[40] N. Todd, S. Moeller, E. J. Auerbach, E. Yacoub, G. Flandin, and N. Weiskopf, “Evaluation of 2D multiband EPI imaging for high-resolution, whole-brain, task-based fMRI studies at 3T: sensitivity and slice leakage artifacts,” *NeuroImage*, vol. 124, pp. 32–42, 2016.
[41] L. Demetriou, O. S. Kowalczyk, G. Tyson, T. Bello, R. D. Newbould, and M. B. Wall, “A comprehensive evaluation of increasing temporal resolution with multiband-accelerated protocols and effects on statistical outcome measures in fMRI,” *NeuroImage*, vol. 176, pp. 404–416, 0 2018, doi: 10.1016/j.neuroimage.2018.05.011.
[42] M. Kiss, P. Hermann, Z. Vidnyánszky, and V. Gál, “Reducing task-based fMRI scanning time using simultaneous multislice echo planar imaging,” *Neuroradiology*, vol. 60, no. 3, pp. 293–302, Mar. 2018, doi: 10.1007/s00234-017-1962-4.
[43] M. A. Griswold *et al.*, “Generalized autocalibrating partially parallel acquisitions (GRAPPA),” *Magnetic Resonance in Medicine*, vol. 47, no. 6, pp. 1202–1210, 2002, doi: 10.1002/mrm.10171.
[44] “Interslice leakage artifact reduction technique for simultaneous multislice acquisitions - Cauley - 2014 - Magnetic Resonance in Medicine - Wiley Online Library.” https://onlinelibrary.wiley.com/doi/full/10.1002/mrm.24898 (accessed May 27, 2020).
[45] T. E. Lund, K. H. Madsen, K. Sidaros, W.-L. Luo, and T. E. Nichols, “Non-white noise in fMRI: Does modelling have an impact?,” *NeuroImage*, vol. 29, no. 1, pp. 54–66, 0 2006, doi: 10.1016/j.neuroimage.2005.07.005.
[46] W. Olszowy, J. Aston, C. Rua, and G. B. Williams, “Accurate autocorrelation modeling substantially improves fMRI reliability,” *Nature Communications*, vol. 10, no. 1, p. 1220, Mar. 2019, doi: 10.1038/s41467-019-09230-w.
[47] N. Corbin, N. Todd, K. J. Friston, and M. F. Callaghan, “Accurate modeling of temporal correlations in rapidly sampled fMRI time series,” *Human Brain Mapping*, vol. 39, no. 10, pp. 3884–3897, 2018, doi: 10.1002/hbm.24218.
[48] V. D. Calhoun, M. C. Stevens, G. D. Pearlson, and K. A. Kiehl, “fMRI analysis with the general linear model: removal of latency-induced amplitude bias by incorporation of hemodynamic derivative terms,” *NeuroImage*, vol. 22, no. 1, pp. 252–257, May 2004, doi: 10.1016/j.neuroimage.2003.12.029.
[49] N. Kanwisher, J. McDermott, and M. M. Chun, “The Fusiform Face Area: A Module in Human Extrastriate Cortex Specialized for Face Perception,” *J. Neurosci.*, vol. 17, no. 11, pp. 4302–4311, Jun. 1997, doi: 10.1523/JNEUROSCI.17-11-04302.1997.
[50] J. V. Haxby, E. A. Hoffman, and M. I. Gobbini, “The distributed human neural system for face perception,” *Trends in Cognitive Sciences*, vol. 4, no. 6, pp. 223–233, Jun. 2000, doi: 10.1016/S1364-6613(00)01482-0.
[51] R. Epstein and N. Kanwisher, “A cortical representation of the local visual environment,” *Nature*, vol. 392, no. 6676, pp. 598–601, Apr. 1998, doi: 10.1038/33402.
[52] P. E. Downing, Y. Jiang, M. Shuman, and N. Kanwisher, “A Cortical Area Selective for Visual Processing of the Human Body,” *Science*, vol. 293, no. 5539, pp. 2470–2473, Sep. 2001, doi: 10.1126/science.1063414.
[53] J. W. Mauchly, “Significance Test for Sphericity of a Normal n-Variate Distribution,” *The Annals of Mathematical Statistics*, vol. 11, no. 2, pp. 204–209, 1940.
[54] S. Geisser and S. W. Greenhouse, “An Extension of Box’s Results on the Use of the F Distribution in Multivariate Analysis,” *Ann. Math. Statist.*, vol. 29, no. 3, pp. 885–891, Sep. 1958, doi: 10.1214/aoms/1177706545.
[55] C. A. Olman, L. Davachi, and S. Inati, “Distortion and Signal Loss in Medial Temporal Lobe,” *PLoS One*, vol. 4, no. 12, Dec. 2009, doi: 10.1371/journal.pone.0008160.
[56] E. M. Aminoff, K. Kveraga, and M. Bar, “The role of the parahippocampal cortex in cognition,” *Trends Cogn Sci*, vol. 17, no. 8, pp. 379–390, Aug. 2013, doi: 10.1016/j.tics.2013.06.009.

[57] O. Baumann and J. B. Mattingley, “Functional Organization of the Parahippocampal Cortex: Dissociable Roles for Context Representations and the Perception of Visual Scenes,” *J. Neurosci.*, vol. 36, no. 8, pp. 2536–2542, Feb. 2016, doi: 10.1523/JNEUROSCI.3368-15.2016.
[58] V. Menon and L. Q. Uddin, “Saliency, switching, attention and control: a network model of insula function,” *Brain Struct Funct*, vol. 214, no. 5–6, pp. 655–667, Jun. 2010, doi: 10.1007/s00429-010-0262-0.
[59] L. Q. Uddin, J. S. Nomi, B. Hebert-Seropian, J. Ghaziri, and O. Boucher, “Structure and function of the human insula,” *J Clin Neurophysiol*, vol. 34, no. 4, pp. 300–306, Jul. 2017, doi: 10.1097/WNP.0000000000000377.

Appendix

Tables A1-A8 represent the results of the multiple comparison analyses on the ROI-averaged adjusted R^2 values based on Tukey's test. The significant results ($p<0.05$) are denoted with asterix and highlighted in bold.

HRF model	MB factor A	MB factor B	Mean Difference (A-B)	Standard Error	Significance (p-value)	95% Confidental Interval	
						Lower Bound	Upper Bound
CAN	MB1	MB4	0.017	0.014	0.477	-0.020	0.053
	MB1	**MB6**	**0.055**	**0.016**	**0.008***	**0.015**	**0.096**
	MB4	**MB6**	**0.039**	**0.011**	**0.009***	**0.010**	**0.068**
DD	MB1	MB4	0.019	0.019	0.590	-0.030	0.068
	MB1	**MB6**	**0.075**	**0.016**	**0.001***	**0.032**	**0.117**
	MB4	**MB6**	**0.056**	**0.014**	**0.003***	**0.020**	**0.091**
FIR	MB1	MB4	-0.003	0.017	0.980	-0.047	0.040
	MB1	**MB6**	**0.062**	**0.013**	**0.001***	**0.028**	**0.096**
	MB4	**MB6**	**0.065**	**0.014**	**0.001***	**0.028**	**0.103**
GAM	MB1	MB4	0.014	0.008	0.212	-0.006	0.034
	MB1	MB6	0.024	0.012	0.138	-0.007	0.055
	MB4	MB6	0.010	0.011	0.621	-0.018	0.038
TD	MB1	MB4	0.009	0.018	0.874	-0.037	0.054
	MB1	**MB6**	**0.062**	**0.014**	**0.001***	**0.026**	**0.098**
	MB4	**MB6**	**0.053**	**0.013**	**0.003***	**0.018**	**0.088**

Table A1. The results of the multiple comparisons for each HRF model within FFA

HRF model	MB factor A	MB factor B	Mean Difference (A-B)	Standard Error	Significance (p-value)	95% Confidental Interval	
						Lower Bound	Upper Bound
CAN	**MB1**	**MB4**	**0.062**	**0.018**	**0.013***	**0.013**	**0.110**
	MB1	**MB6**	**0.096**	**0.020**	**0.001***	**0.044**	**0.148**
	MB4	MB6	0.035	0.014	0.062	-0.002	0.071
DD	**MB1**	**MB4**	**0.079**	**0.021**	**0.007***	**0.022**	**0.135**
	MB1	**MB6**	**0.127**	**0.020**	**<0.001***	**0.075**	**0.179**
	MB4	MB6	0.049	0.015	**0.018***	0.008	0.089
FIR	MB1	MB4	0.026	0.021	0.437	-0.028	0.081
	MB1	**MB6**	**0.082**	**0.017**	**0.001***	**0.036**	**0.127**
	MB4	**MB6**	**0.055**	**0.016**	**0.011***	**0.013**	**0.098**
GAM	MB1	MB4	0.016	0.013	0.481	-0.019	0.051
	MB1	**MB6**	**0.039**	**0.014**	**0.042***	**0.001**	**0.078**
	MB4	**MB6**	**0.024**	**0.016**	**0.345**	**-0.019**	**0.067**
TD	MB1	MB4	0.044	0.026	0.233	-0.024	0.112
	MB1	**MB6**	**0.110**	**0.019**	**<0.001***	**0.061**	**0.160**
	MB4	MB6	0.066	0.026	0.060	-0.003	0.135

Table A2. The results of the multiple comparisons for each HRF model within OFA

HRF model	MB factor A	MB factor B	Mean Difference (A-B)	Standard Error	Significance (p-value)	95% Confidental Interval	
						Lower Bound	Upper Bound
CAN	MB1	MB4	0.001	0.006	0.978	-0.014	0.016
	MB1	**MB6**	**0.036**	**0.009**	**0.003***	**0.013**	**0.059**
	MB4	**MB6**	**0.034**	**0.008**	**0.001***	**0.014**	**0.055**
DD	MB1	MB4	0.006	0.008	0.754	-0.015	0.027
	MB1	**MB6**	**0.056**	**0.010**	**<0.001***	**0.029**	**0.083**
	MB4	**MB6**	**0.050**	**0.009**	**<0.001***	**0.026**	**0.074**
FIR	MB1	MB4	-0.010	0.007	0.376	-0.027	0.008
	MB1	**MB6**	**0.043**	**0.008**	**<0.001***	**0.022**	**0.064**
	MB4	**MB6**	**0.053**	**0.009**	**<0.001***	**0.029**	**0.076**
GAM	MB1	MB4	0.001	0.005	0.993	-0.013	0.014
	MB1	**MB6**	**0.024**	**0.006**	**0.001**	**0.010**	**0.039**
	MB4	**MB6**	**0.024**	**0.005**	**0.001**	**0.011**	**0.037**
TD	MB1	MB4	0.001	0.008	0.998	-0.022	0.021
	MB1	**MB6**	**0.047**	**0.008**	**<0.001***	**0.026**	**0.069**
	MB4	**MB6**	**0.048**	**0.008**	**<0.001***	**0.026**	**0.069**

Table A3. The results of the multiple comparisons for each HRF model within PPA

HRF model	MB factor A	MB factor B	Mean Difference (A-B)	Standard Error	Significance (p-value)	95% Confidental Interval	
						Lower Bound	Upper Bound
CAN	MB1	MB4	0.029	0.020	0.331	-0.022	0.080
	MB1	**MB6**	**0.072**	**0.021**	**0.010***	**0.017**	**0.128**
	MB4	**MB6**	**0.043**	**0.015**	**0.025***	**0.005**	**0.081**
DD	MB1	MB4	0.039	0.021	0.187	-0.016	0.094
	MB1	**MB6**	**0.104**	**0.020**	**<0.001***	**0.052**	**0.156**
	MB4	**MB6**	**0.065**	**0.014**	**0.001***	**0.027**	**0.102**
FIR	MB1	MB4	-0.003	0.021	0.991	-0.056	0.050
	MB1	**MB6**	**0.078**	**0.019**	**0.002**	**0.029**	**0.127**
	MB4	**MB6**	**0.081**	**0.017**	**<0.001***	**0.038**	**0.124**
GAM	MB1	MB4	0.017	0.011	0.259	-0.010	0.045
	MB1	**MB6**	**0.041**	**0.015**	**0.036***	**0.002**	**0.079**
	MB4	MB6	0.023	0.014	0.239	-0.012	0.059
TD	MB1	MB4	0.023	0.019	0.464	-0.026	0.073
	MB1	**MB6**	**0.084**	**0.018**	**0.001***	**0.039**	**0.130**
	MB4	**MB6**	**0.061**	**0.015**	**0.002***	**0.024**	**0.099**

Table A4. The results of the multiple comparisons for each HRF model within EBA

MB factor	HRF model A	HRF model B	Mean Difference (A-B)	Standard Error	Significance (p-value)	95% Confidental Interval	
						Lower Bound	Upper Bound
MB1	**CAN**	**DD**	**-0.030**	**0.005**	**<0.001***	**-0.046**	**-0.014**
	CAN	FIR	-0.010	0.004	0.082	-0.021	0.001
	CAN	**GAMMA**	**0.038**	**0.007**	**0.001***	**0.015**	**0.061**
	CAN	**TD**	**-0.018**	**0.003**	**<0.001***	**-0.027**	**-0.008**
	DD	**FIR**	**0.020**	**0.005**	**0.010***	**0.004**	**0.036**
	DD	**GAMMA**	**0.068**	**0.011**	**<0.001***	**0.035**	**0.101**
	DD	**TD**	**0.013**	**0.003**	**0.004***	**0.004**	**0.021**
	FIR	**GAMMA**	**0.048**	**0.007**	**<0.001***	**0.026**	**0.070**
	FIR	TD	-0.008	0.004	0.264	-0.019	0.003
	GAMMA	**TD**	**-0.055**	**0.008**	**<0.001***	**-0.081**	**-0.029**
MB4	**CAN**	**DD**	**-0.028**	**0.005**	**0.001***	**-0.044**	**-0.012**
	CAN	**FIR**	**-0.030**	**0.006**	**0.002***	**-0.049**	**-0.011**
	CAN	**GAMMA**	**0.035**	**0.008**	**0.007***	**0.009**	**0.061**
	CAN	**TD**	**-0.026**	**0.007**	**0.024***	**-0.048**	**-0.003**
	DD	FIR	-0.002	0.003	0.947	-0.011	0.007
	DD	**GAMMA**	**0.063**	**0.012**	**0.001***	**0.026**	**0.100**
	DD	TD	0.002	0.008	0.998	-0.021	0.026
	FIR	**GAMMA**	**0.065**	**0.012**	**0.001***	**0.028**	**0.102**
	FIR	TD	0.004	0.006	0.953	-0.015	0.024
	GAMMA	**TD**	**-0.060**	**0.011**	**<0.001***	**-0.093**	**-0.028**
MB6	CAN	DD	-0.011	0.007	0.546	-0.033	0.011
	CAN	FIR	-0.004	0.007	0.982	-0.024	0.017
	CAN	GAMMA	0.006	0.007	0.915	-0.017	0.029
	CAN	TD	-0.011	0.009	0.705	-0.038	0.016
	DD	**FIR**	**0.007**	**0.002**	**0.016***	**0.001**	**0.014**
	DD	GAMMA	0.017	0.008	0.235	-0.007	0.041
	DD	TD	0.001	0.005	0.998	-0.015	0.015
	FIR	GAMMA	0.010	0.008	0.745	-0.015	0.035
	FIR	TD	-0.007	0.005	0.561	-0.023	0.008
	GAMMA	TD	-0.017	0.007	0.187	-0.040	0.006

Table A5. The results of the multiple comparisons for each MB factor models within FFA

MB factor	HRF model A	HRF model B	Mean Difference (A-B)	Standard Error	Significance (p-value)	95% Confidental Interval	
						Lower Bound	Upper Bound
MB1	**CAN**	**DD**	**-0.030**	**0.005**	**<0.001***	**-0.046**	**-0.014**
	CAN	FIR	-0.010	0.004	0.082	-0.021	0.001
	CAN	**GAMMA**	**0.038**	**0.007**	**0.001***	**0.015**	**0.061**
	CAN	**TD**	**-0.018**	**0.003**	**<0.001***	**-0.027**	**-0.008**
	DD	**FIR**	**0.020**	**0.005**	**0.010**	**0.004**	**0.036**
	DD	**GAMMA**	**0.068**	**0.011**	**<0.001***	**0.035**	**0.101**
	DD	**TD**	**0.013**	**0.003**	**0.004**	**0.004**	**0.021**
	FIR	**GAMMA**	**0.048**	**0.007**	**<0.001***	**0.026**	**0.070**
	FIR	TD	-0.008	0.004	0.264	-0.019	0.003
	GAMMA	**TD**	**-0.055**	**0.008**	**<0.001***	**-0.081**	**-0.029**
MB4	**CAN**	**DD**	**-0.028**	**0.005**	**0.001***	**-0.044**	**-0.012**
	CAN	**FIR**	**-0.030**	**0.006**	**0.002***	**-0.049**	**-0.011**
	CAN	**GAMMA**	**0.035**	**0.008**	**0.007***	**0.009**	**0.061**
	CAN	**TD**	**-0.026**	**0.007**	**0.024***	**-0.048**	**-0.003**
	DD	FIR	-0.002	0.003	0.947	-0.011	0.007
	DD	**GAMMA**	**0.063**	**0.012**	**0.001***	**0.026**	**0.100**
	DD	TD	0.002	0.008	0.998	-0.021	0.026
	FIR	**GAMMA**	**0.065**	**0.012**	**0.001***	**0.028**	**0.102**
	FIR	TD	0.004	0.006	0.953	-0.015	0.024
	GAMMA	**TD**	**-0.060**	**0.011**	**<0.001***	**-0.093**	**-0.028**
MB6	CAN	DD	-0.011	0.007	0.546	-0.033	0.011
	CAN	FIR	-0.004	0.007	0.982	-0.024	0.017
	CAN	GAMMA	0.006	0.007	0.915	-0.017	0.029
	CAN	TD	-0.011	0.009	0.705	-0.038	0.016
	DD	**FIR**	**0.007**	**0.002**	**0.016***	**0.001**	**0.014**
	DD	GAMMA	0.017	0.008	0.235	-0.007	0.041
	DD	TD	0.001	0.005	0.998	-0.015	0.015
	FIR	GAMMA	0.010	0.008	0.745	-0.015	0.035
	FIR	TD	-0.007	0.005	0.561	-0.023	0.008
	GAMMA	TD	-0.017	0.007	0.187	-0.040	0.006

Table A6. The results of the multiple comparisons for each MB factor models within OFA

MB factor	HRF model A	HRF model B	Mean Difference (A-B)	Standard Error	Significance (p-value)	95% Confidental Interval	
						Lower Bound	Upper Bound
MB1	**CAN**	**DD**	**-0.031**	**0.006**	**0.001***	**-0.049**	**-0.012**
	CAN	**FIR**	**-0.018**	**0.006**	**0.035***	**-0.035**	**-0.001**
	CAN	GAMMA	0.017	0.008	0.265	-0.008	0.042
	CAN	**TD**	**-0.021**	**0.006**	**0.013***	**-0.038**	**-0.004**
	DD	**FIR**	**0.013**	**0.004**	**0.046***	**0.000**	**0.025**
	DD	**GAMMA**	**0.047**	**0.008**	**<0.001***	**0.022**	**0.073**
	DD	**TD**	**0.010**	**0.003**	**0.031***	**0.001**	**0.018**
	FIR	**GAMMA**	**0.035**	**0.006**	**<0.001***	**0.016**	**0.053**
	FIR	TD	-0.003	0.003	0.892	-0.013	0.007
	GAMMA	**TD**	**-0.038**	**0.006**	**<0.001***	**-0.056**	**-0.020**
MB4	**CAN**	**DD**	**-0.026**	**0.006**	**0.005***	**-0.044**	**-0.007**
	CAN	**FIR**	**-0.029**	**0.006**	**0.001***	**-0.046**	**-0.011**
	CAN	GAMMA	0.016	0.009	0.342	-0.010	0.043
	CAN	**TD**	**-0.022**	**0.006**	**0.014***	**-0.040**	**-0.004**
	DD	FIR	-0.003	0.003	0.821	-0.011	0.005
	DD	**GAMMA**	**0.042**	**0.008**	**0.001***	**0.018**	**0.067**
	DD	TD	0.003	0.004	0.877	-0.008	0.015
	FIR	**GAMMA**	**0.045**	**0.007**	**<0.001***	**0.024**	**0.066**
	FIR	TD	0.006	0.003	0.130	-0.001	0.014
	GAMMA	**TD**	**-0.039**	**0.007**	**<0.001***	**-0.059**	**-0.018**
MB6	**CAN**	**DD**	**-0.010**	**0.002**	**<0.001***	**-0.015**	**-0.005**
	CAN	**FIR**	**-0.010**	**0.002**	**<0.001***	**-0.016**	**-0.005**
	CAN	GAMMA	0.006	0.003	0.292	-0.003	0.015
	CAN	**TD**	**-0.009**	**0.002**	**0.005***	**-0.016**	**-0.002**
	DD	FIR	0.000	0.001	0.999	-0.005	0.004
	DD	**GAMMA**	**0.016**	**0.003**	**0.002***	**0.006**	**0.026**
	DD	TD	0.001	0.002	0.983	-0.005	0.007
	FIR	DD	0.000	0.001	0.999	-0.004	0.005
	FIR	**GAMMA**	**0.016**	**0.002**	**<0.001***	**0.009**	**0.024**
	GAMMA	**TD**	**-0.015**	**0.003**	**0.002***	**-0.025**	**-0.005**

Table A7. The results of the multiple comparisons for each MB factor within PPA

MB factor	HRF model A	HRF model B	Mean Difference (A-B)	Standard Error	Significance (p-value)	95% Confidental Interval	
						Lower Bound	Upper Bound
MB1	**CAN**	**DD**	**-0.047**	**0.009**	**0.001***	**-0.076**	**-0.018**
	CAN	FIR	-0.013	0.008	0.583	-0.038	0.013
	CAN	**GAMMA**	**0.058**	**0.016**	**0.016***	**0.009**	**0.106**
	CAN	**TD**	**-0.025**	**0.008**	**0.034***	**-0.048**	**-0.002**
	DD	**FIR**	**0.035**	**0.006**	**<0.001***	**0.017**	**0.053**
	DD	**GAMMA**	**0.105**	**0.018**	**<0.001***	**0.049**	**0.160**
	DD	**TD**	**0.022**	**0.004**	**<0.001***	**0.010**	**0.035**
	FIR	GAMMA	0.070	0.015	0.002*	0.024	0.116
	FIR	TD	-0.012	0.004	0.086	-0.026	0.001
	GAMMA	**TD**	**-0.083**	**0.014**	**<0.001***	**-0.127**	**-0.038**
MB4	**CAN**	**DD**	**-0.037**	**0.007**	**<0.001**	**-0.057**	**-0.016**
	CAN	**FIR**	**-0.044**	**0.007**	**<0.001***	**-0.066**	**-0.023**
	CAN	**GAMMA**	**0.046**	**0.014**	**<0.025**	**0.005**	**0.088**
	CAN	**TD**	**-0.031**	**0.006**	**<0.002***	**-0.050**	**-0.011**
	DD	FIR	-0.007	0.006	0.774	-0.027	0.012
	DD	**GAMMA**	**0.083**	**0.018**	**0.002***	**0.028**	**0.138**
	DD	TD	0.006	0.007	0.908	-0.016	0.028
	FIR	**GAMMA**	**0.090**	**0.017**	**0.001**	**0.038**	**0.143**
	FIR	TD	0.014	0.007	0.341	-0.008	0.035
	GAMMA	**TD**	**-0.077**	**0.015**	**0.001***	**-0.122**	**-0.032**
MB6	CAN	DD	-0.015	0.007	0.245	-0.037	0.006
	CAN	FIR	-0.007	0.007	0.863	-0.028	0.014
	CAN	GAMMA	0.026	0.010	0.095	-0.003	0.055
	CAN	TD	-0.013	0.010	0.720	-0.044	0.018
	DD	**FIR**	**0.009**	**0.003**	**0.026***	**0.001**	**0.017**
	DD	**GAMMA**	**0.042**	**0.008**	**0.001***	**0.017**	**0.066**
	DD	TD	0.003	0.006	0.993	-0.017	0.022
	FIR	**GAMMA**	**0.033**	**0.008**	**0.004***	**0.010**	**0.056**
	FIR	TD	-0.006	0.006	0.850	-0.025	0.013
	GAMMA	**TD**	**-0.039**	**0.008**	**0.002***	**-0.064**	**-0.014**

Table A8. The results of the multiple comparison Analysis for each MB factor within EBA